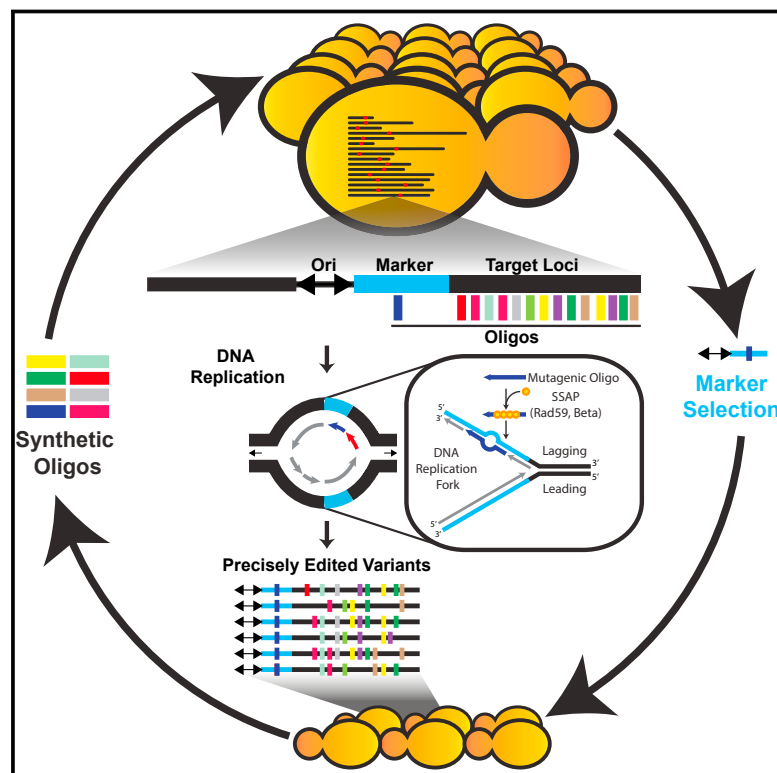


# Precise Editing at DNA Replication Forks Enables Multiplex Genome Engineering in Eukaryotes

## Graphical Abstract



## Authors

Edward M. Barbieri, Paul Muir, Benjamin O. Akhuetie-Oni, Christopher M. Yellman, Farren J. Isaacs

## Correspondence

farren.isaacs@yale.edu

## In Brief

Replication forks can be co-opted to introduce multisite mutations in eukaryotic genomes without the need for DNA double-strand break.

## Highlights

- Yeast multiplex genome engineering technology that avoids DNA double-strand breaks
- Rad51-independent mechanism of gene editing by ssODN annealing at DNA replication
- Silencing DNA repair and slowing replication enhances multiplex editing by ssODNs
- Generation of combinatorial genetic variants at base-pair precision in eukaryotes

# Precise Editing at DNA Replication Forks Enables Multiplex Genome Engineering in Eukaryotes

Edward M. Barbieri,<sup>1,2</sup> Paul Muir,<sup>1,2</sup> Benjamin O. Akhuetie-Oni,<sup>1,2</sup> Christopher M. Yellman,<sup>1,2,3</sup> and Farren J. Isaacs<sup>1,2,4,\*</sup>

<sup>1</sup>Department of Molecular, Cellular, & Developmental Biology, Yale University, New Haven, CT 06520, USA

<sup>2</sup>Systems Biology Institute, Yale University, West Haven, CT 06516, USA

<sup>3</sup>Present address: Center for Systems and Synthetic Biology, The University of Texas at Austin, Austin, TX 78712, USA

<sup>4</sup>Lead Contact

\*Correspondence: [farren.isaacs@yale.edu](mailto:farren.isaacs@yale.edu)

<https://doi.org/10.1016/j.cell.2017.10.034>

## SUMMARY

We describe a multiplex genome engineering technology in *Saccharomyces cerevisiae* based on annealing synthetic oligonucleotides at the lagging strand of DNA replication. The mechanism is independent of Rad51-directed homologous recombination and avoids the creation of double-strand DNA breaks, enabling precise chromosome modifications at single base-pair resolution with an efficiency of >40%, without unintended mutagenic changes at the targeted genetic loci. We observed the simultaneous incorporation of up to 12 oligonucleotides with as many as 60 targeted mutations in one transformation. Iterative transformations of a complex pool of oligonucleotides rapidly produced large combinatorial genomic diversity >10<sup>5</sup>. This method was used to diversify a heterologous  $\beta$ -carotene biosynthetic pathway that produced genetic variants with precise mutations in promoters, genes, and terminators, leading to altered carotenoid levels. Our approach of engineering the conserved processes of DNA replication, repair, and recombination could be automated and establishes a general strategy for multiplex combinatorial genome engineering in eukaryotes.

## INTRODUCTION

Most eukaryotic genome-editing technologies—zinc-finger nucleases (ZFNs), transcription activator-like effector nucleases (TALENs), and CRISPR-Cas9—generate DNA double-strand breaks (DSBs) at targeted loci to introduce genomic modifications (Chandrasegaran and Carroll, 2016; Doudna and Charpentier, 2014). Although ZFNs and TALENs recognize specific DNA sequences through protein-DNA interactions and use the *FokI* nuclease domain to introduce DSBs at genomic loci, construction of functional ZFNs and TALENs with desired DNA specificity remains laborious, costly, and primarily limited to modifications at a single locus. CRISPR-Cas9 has been broadly adopted for multiplexed targeting of genomic modifications because the

nuclease Cas9 uses a short guide RNA to recognize the target DNA via Watson-Crick base-pairing (Jinek et al., 2012) and has been shown to function in many organisms (Cong et al., 2013; Mali et al., 2013). CRISPR-Cas9 is suited for gene disruption applications by non-homologous end joining (NHEJ) (Yang et al., 2015) and gene editing via homology-directed repair (HDR) (Doudna and Charpentier, 2014).

For applications that require multisite editing or precise base-pair (bp)-level genome modifications by HDR, the DSB mechanism is limiting for three key reasons. First, cleaving the genome is cytotoxic, and cell lethality is magnified when DSBs are introduced across multiple target sites (Jakočiūnas et al., 2015). Second, in eukaryotes most single bp HDR changes introduced by DSB repair are subject to additional unwanted insertions or deletions (indels) resulting from NHEJ (Inui et al., 2014). These additional mutations result from high tolerance of the targeted nuclease (i.e., Cas9:gRNA [guide RNA]) to mismatches in the DSB target, which can lead to additional cleavage even after HDR editing has occurred (Fu et al., 2013). For single-bp HDR, the inclusion of blocking mutations in the donor DNA is typically required to mask the genomic target site from further cutting by the Cas9:gRNA (Horwitz et al., 2015; Paquet et al., 2016). For many types of genetic elements (e.g., promoters, ncRNAs), the exact DNA sequence dictates function such that additional blocking mutations can be prohibitive. Despite the improved stringencies of engineered Cas9 variants, mismatches are still tolerated for many nonstandard target sites with repetitive regions (Tsai and Joung, 2016). Third, the inefficiency of generating targeted single-bp edits with DSBs limits the ability to simultaneously modify many loci in a single cell or across a population to produce combinatorial genetic diversity for exploration of vast genomic landscapes. Efficient DNA base editing without a DSB has been reported using Cas9-guided deamination, but this technique is limited to specific C  $\rightarrow$  T or G  $\rightarrow$  A mutations in an imprecise window of several bps (Komor et al., 2016). Thus, creating precise edits at single-bp resolution remains a defining challenge for eukaryotic genome engineering technologies.

Prior work in *Escherichia coli* demonstrated that targeted chromosomal modifications could be introduced without DSBs using synthetic single-stranded DNA (ssDNA) oligodeoxynucleotides (ssODNs) complementary to the lagging strand of the replicating chromosome. High efficiencies (>10%) were achieved by using the phage  $\lambda$  Red Beta ssDNA annealing protein (SSAP) to

facilitate ssODN annealing at the lagging strand during DNA replication (Costantino and Court, 2003). With the advent of multiplex automated genome engineering (MAGE), this approach was enhanced to generate multisite genome modifications with bp precision at increased efficiencies (>30%) and used for pathway diversification (Wang et al., 2009), whole-genomic recoding (Lajoie et al., 2013), and molecular evolution of proteins (Amiram et al., 2015). In *S. cerevisiae*, homologous recombination (HR) of ssODNs results in low gene targeting efficiencies ( $\sim 10^{-4}\%$ – $10^{-3}\%$ ), which limits the scope of applications to single locus modifications (Kow et al., 2007; Storici and Resnick, 2003). The mechanism of ssODN incorporation in eukaryotic cells is not precisely defined and may involve several factors, which include direction of DNA replication, cell-cycle phase, transcription, DNA mismatch repair (MMR), and HR (Rivera-Torres and Kmiec, 2016). Efforts to develop an analogous MAGE technology in *S. cerevisiae* have focused on overexpression of HR factors Rad51 and Rad54 in MMR deficient strains and resulted in moderately enhanced allelic replacement frequencies (ARFs) ( $\sim 0.1\%$ – $2\%$ ) (DiCarlo et al., 2013). Thus, no method has been established in eukaryotes for precise, multisite genome modification with ssODNs at efficiencies attained in *E. coli*.

Here, we describe eukaryotic MAGE (eMAGE) for the generation of precise combinatorial genome modifications of the model eukaryote and industrial chassis organism *S. cerevisiae*. This approach is rooted in biasing the annealing of synthetic ssODNs during DNA replication rather than a Rad51-directed strand-invasion mechanism. We observe single-bp precision gene editing with efficiencies >40%. Since eMAGE does not rely on DSBs, the process is highly scalable across a genomic region of interest and can simultaneously generate many precise and diverse modifications of a chromosome. We demonstrate that combinatorial genomic diversity can be generated across a population of cells in a single transformation, genomic landscapes can be traversed through successive iterations of this process, and multiple distal genetic changes can be parallelized and combined through strain mating to sample new phenotypes.

## RESULTS

### Engineering ssODN Annealing at DNA Replication Forks

Recombinase proteins (e.g., Rad51) catalyze the pairing and exchange of homologous DNA sequences. In *S. cerevisiae*, additional factors (e.g., Rad52, Rad54, Rad55, Rad57, and Rad59) participate in HR by promoting the formation of Rad51-ssDNA filaments or through annealing of ssDNA (San Filippo et al., 2008). Prior work proposed that ssODNs are incorporated in the yeast genome through Rad51-mediated HR (Figure 1A) (DiCarlo et al., 2013; Liu et al., 2004). Along these lines, we tried to enhance ssODN-mediated recombination by increasing expression of HR genes and impairing MMR. We measured ARF for an ssODN containing a single bp mutation in the *RPL28* gene, which confers cycloheximide resistance, for a panel of HR genes and MMR knockout (KO) strains (Figures 1B, S1A, and S1B). Overexpression of the three HR factors Rad51, Rad52, and Rad59 increased ARF at least 10-fold above the negative control, with Rad51 and Rad52 producing the high-

est ARF (0.02%), followed by Rad59 (0.01%). Ablation of MMR led to  $\sim 100$ -fold enhancement (0.1%) in the strain *msh2 $\Delta$* . Next, we combined HR overexpression with MMR KO strains (Figures 1B and S1C–S1F). Overexpression of Rad51 in *msh2 $\Delta$* , *msh6 $\Delta$* , and *mlh1 $\Delta$*  strains increased ARF 4-fold above the level of the *msh2 $\Delta$*  strain alone, yielding a maximum ARF of 0.4% that is consistent with prior work (DiCarlo et al., 2013). Together, these data suggest that ssODN incorporation by promoting Rad51-dependent HR and disabling MMR may be limited to the ARF previously reported.

We hypothesized that Rad51-dependent ssODN recombination and incorporation of ssODNs at the DNA replication fork are two distinct pathways in eukaryotes (Figure 1A). Sherman and colleagues observed high frequencies of co-transformation for two ssODNs targeted within a *cyc1* mutant gene when one of the ssODNs included a selectable mutation (Yamamoto et al., 1992), which suggests that the two ssODNs were incorporated at the same DNA replication fork, and a finding also observed in *E. coli* (Carr et al., 2012). To test ssODN gene editing at the replication fork, we constructed an experimental locus on chromosome 15 with a defined DNA replication direction by placing *URA3* proximal to the origin of replication ARS1516 (Ori) directly adjacent to *ADE2*, which confers a colorimetric phenotype (wild-type [WT], white; mutant, red) (Figure 1C). We transformed cells with ssODNs targeting the predicted lagging strand of both *URA3* and *ADE2* and assayed the frequency of *ade2* colony-forming units (CFUs). We did not detect *ade2* CFUs for the WT strain (limit of detection [LOD] =  $10^{-4}$  CFU), and we observed  $\sim 0.1\%$  *ade2* CFUs for *msh2 $\Delta$*  (Figure 1D). After 5-FOA selection to enrich for a competent subpopulation in *ura3* clones, we observed 22% and 27% of CFUs with ssODN-derived *ade2* mutations for WT and *msh2 $\Delta$* , respectively. To determine if the ARF enhancement is due to a coupled replication fork annealing mechanism we tested a marker-target pair (*RPL28-ADE2*) separated on different chromosomes (Figures S1G and S1H). After selection for *rpl28* mutants, we recovered *ade2* mutants in only 0.4% of CFUs, and overexpression of Rad51 led to a  $\sim 100\%$  increase (0.8%). Thus, ssODN incorporation is enhanced in *ura3*-edited competent cells where downstream modifications are kinetically favored along a DNA replication fork in a localized chromosomal region.

To assess the impact of HR factors on the proposed replication fork annealing mechanism, we created a set of KO and overexpression strains for HR genes and assayed ssODN incorporation at the Ori-*URA3-ADE2* locus. Unlike the *RPL28-ADE2* interchromosomal pair, overexpression of Rad51 decreased ARF from  $\sim 22\%$  to  $\sim 5\%$ , whereas deletion of Rad51 increased ARF to  $\sim 30\%$  (Figure 1E). Application of the Rad51 inhibitor RI-1 also enhanced ARF (Figure S1I). Overexpression of the SSAP Rad52 increased ARF to  $\sim 29\%$ , whereas deletion of Rad52 showed a neutral effect. Overexpression of the SSAP Rad59 decreased ARF to  $\sim 16\%$ , whereas we did not observe *ade2* mutants in *rad59 $\Delta$*  (LOD =  $10^{-3}$  CFU). The effect of *rad59 $\Delta$*  was epistatic to *rad52 $\Delta$*  (*rad52 $\Delta$ rad59 $\Delta$* ). We observed varying degrees of suppression of *rad59 $\Delta$*  and *rad52 $\Delta$ rad59 $\Delta$*  with overexpression of Rad51, Rad52, Rad59, or  $\lambda$  Red Beta. Since loss of Rad52 impairs Rad51-dependent HR (Sung, 1997), we observed a higher ARF with Rad51 overexpression in *rad59 $\Delta$*  (4.6%) than

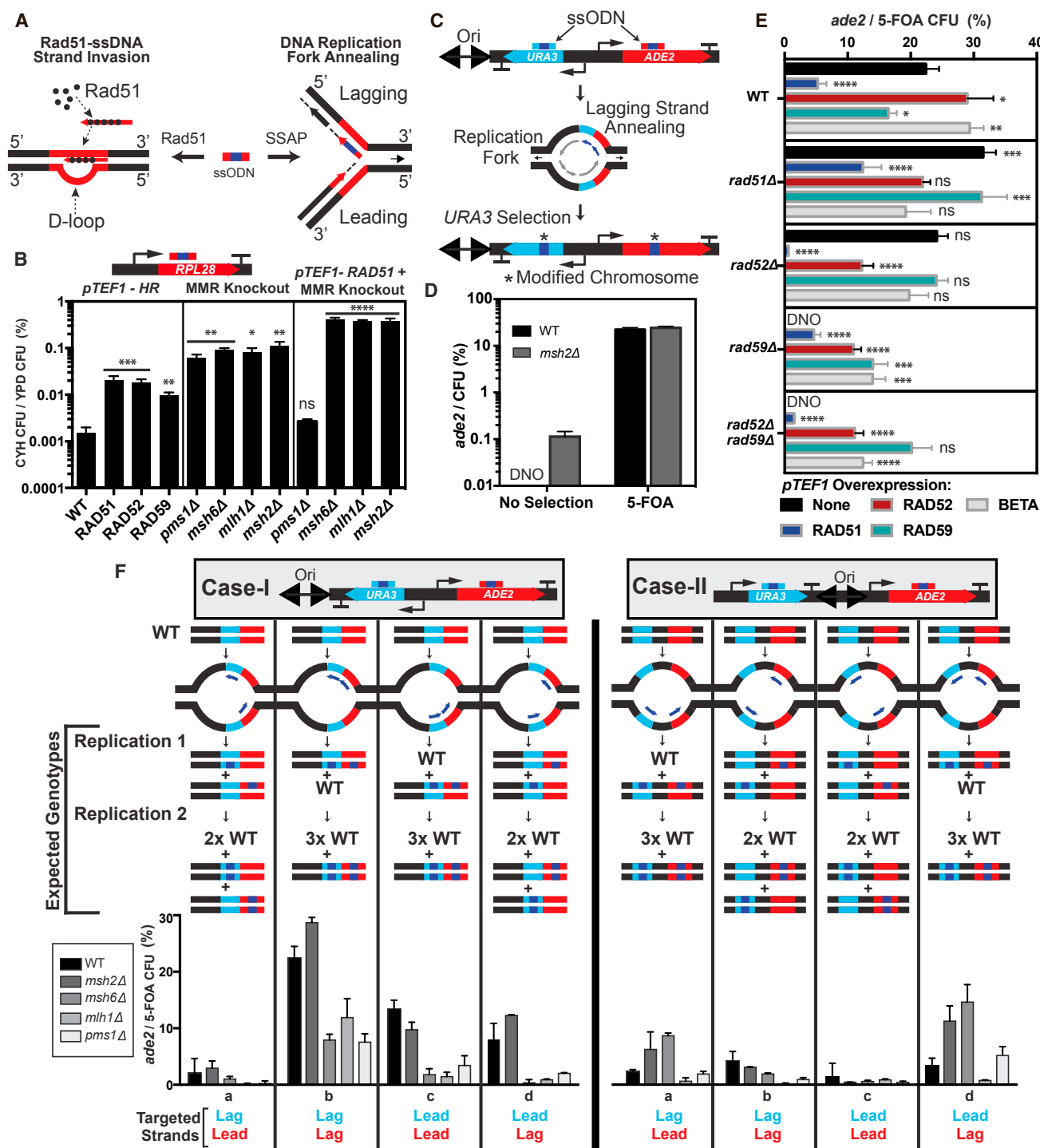


**Figure 1. Engineering ssODN Incorporation at DNA Replication Forks**

(A) Two pathways for ssODN incorporation in the genome. Rad51-dependent ssDNA strand invasion and SSAP-dependent annealing of ssODNs at the replication fork.

(B) ARFs for ssODNs with *pTEF1* overexpression of HR genes (capitalized), MMR KO strains, and combinations of *pTEF1*-RAD51 and MMR KO.

(C) Schematic for selection of ssODN annealing at the replication fork.

(D) Measurement of *ADE2* ARFs after transformation with *ura3* and *ade2* ssODNs in WT and *msh2Δ* on non-selection and 5-FOA selection plates.

(E) WT and HR KO strains + overexpression of the indicated gene. DNO, did not observe.

(legend continued on next page)

*rad52Δ* (0.6%) or *rad52Δrad59Δ* (1.5%). Overexpression of Rad52 showed an equivalent ARF in all three strains (~10%). The effect of Rad59 overexpression was enhanced in *rad51Δ*, *rad52Δ*, and *rad52Δrad59Δ*, potentially because of reduced competition from Rad51-dependent HR in these strains. Notably, λ Red Beta enhanced ARF to ~29% in WT and recovered *rad59Δ* and *rad52Δrad59Δ* to ~13%. In summary, our data show that ssODN annealing at the replication fork is distinct from Rad51-mediated ssODN recombination, enhanced in the *rad51Δ* background, and requires an SSAP (e.g., Rad59, Beta).

To further study ssODN annealing at the replication fork, we tested the effect of leading (lead) versus lagging (lag) strand targeting. Since yeast chromosomes contain multiple origins of replication that fire at varying efficiencies (Friedman et al., 1997), we placed *URA3* in two orientations with respect to *ADE2* (Figure 1F). In case 1, *URA3* and *ADE2* reside on the same side of the Ori, such that they are replicated in the same replication fork. In case 2, *URA3* and *ADE2* are positioned on different sides of the Ori, such that they are replicated in opposing directions when the Ori fires. We tested all lead/lag strand combinations in a set of WT (BY4741) and MMR mutant strains (*msh2Δ*, *msh6Δ*, *mlh1Δ*, and *pms1Δ*). The WT and *msh2Δ* strains had the highest ARF; however, the number of 5-FOA-resistant CFUs was ~100-fold higher for *msh2Δ* compared to WT (see Figure 1B). In addition to selection for competent cells (Figure 1D), we observed two key factors that enhance ARF: (1) ssODNs that target the lag strand and (2) ssODN pairs that target the same chromosomal strand. The lag strand is favorable because of the prevalence of available ssDNA compared to the lead strand (Rivera-Torres and Kmiec, 2016) and pairs of ssODNs that target the same chromosomal strand result in cosegregation of the ssODN-derived alleles. Consistent with this model, the lag-lag (*ura3-ade2*) strand combination for case 1 (case 1b) satisfies both criteria and showed the highest ARF in all strains except *msh6Δ*, which was enhanced in case 2. Such differences in ARF could be due to MMR activity at the replisome or altered replisome dynamics and warrants investigation in future work. Cases 1c (lead-lead), 2a (lag-lead), and 2d (lead-lag) satisfy condition 2 and showed elevated ARF. Since the Ori does not always fire, the enhanced ARF for cases 2a and 2d could be explained by replication from adjacent origins in some cells rendering the ssODNs in the same replication fork. Four scenarios (cases 1a, 1d, 2b, and 2c) should not result in cosegregation of the *ura3* and *ade2* alleles, yet we observed clones with both ssODN-derived alleles. This suggests that either the ssODNs can persist for more than a single cell cycle or rapid processing of the heteroduplex by MMR or a MMR-independent pathway followed by HR between sister chromatids might explain the cosegregation (San Filippo et al., 2008). For these scenarios, higher ARFs occur when the *ade2* ssODN is targeted to the lag strand. To validate our findings, we observed equivalent strand bias trends for

*msh2Δ* in both case 1 and case 2 for a distal locus (*RPL28*) on chromosome 7 (Figure S1J). Thus, efficient ssODN incorporation (>10%) can be achieved for marker-target pairs adjacent to or on opposite sides of an Ori through precise targeting at the replication fork.

### Investigating Replication and Repair Factors for ssODN Incorporation

We conducted three key experiments to investigate the impact of replication dynamics and factors that monitor replication and repair. First, we tested if slowing DNA replication with hydroxyurea (HU) enhances ssODN incorporation. A 30-min treatment with 500 mM HU increased the ARF by ~2-fold with no significant increase in spontaneous *ura3* mutations (Figures S2A and S2B). HU also enhanced ARF by an average of 56% for seven ssODNs containing a single bp mismatch (ssODNs 1, 2, and 5–7), insertion (ssODN 4), or deletion (ssODN 3) in *ADE2* (Figure 2A). To validate these data and disconnect the selection step from dNTP metabolism, we observed similar findings with *HIS3* selection (Figure S2C). Next, to determine if annealing of the *ura3* ssODN induces a DNA damage response that enhances downstream ssODN annealing, we exposed cells to a range of UV irradiation, a general DNA damage event, and did not observe an ARF increase (Figure S2D). Third, replication slowing has been implicated to occur during gene editing (Rivera-Torres and Kmiec, 2016), and we postulated that ssODN annealing might stall the replication fork to enhance ARFs at downstream loci. Since Mec1-dependent signaling is associated with stalled replication forks (Branzei and Foiani, 2010), we tested the effect of deleting Mec1 (Figure 2B). Given that null mutants of Mec1 are viable in *smf1Δ* strains, we measured ARF in *smf1Δ* and *smf1Δmec1Δ*. ARF was reduced by ~25% in *smf1Δ* and by ~60% in *smf1Δmec1Δ* for both ± HU conditions. In summary, slowing replication fork speed with HU increases ARF; ARF enhancement is independent of UV-induced DNA damage; and Mec1 deletion attenuates ARF.

### Optimizing Parameters to Enhance Genome Editing

To maximize ARFs, we performed a set of experiments to identify the optimal size and concentration of ssODNs in *msh2Δ* using 500 mM HU. Given that cell survival is crucial for generating large mutant libraries, we tested the effect of increasing ssODN concentration on cell survival 1 hr post-electroporation, allowing for cell recovery below the doubling-time (>100-min for *msh2Δ*). Robust survival (85%) was obtained for ssODN concentrations from 0 to 20 μM, which decreased to 45% at 80 μM ssODN (Figure S2E). We also tested the effect of ssODN size (50–100 nt) and concentration (0.1–60 μM) on the ARF for single (*ura3*) and double (*ura3-ade2*) ssODN incorporation. The efficiency of *ura3* mutants increased with increasing ssODN size and concentration with the highest ARF observed (0.08%) for 100 nt ssODN at 60 μM (Figure S1F). For coupled *ura3-ade2*

(F) Two cases for *URA3* and *ADE2* orientation at the Ori. Diagrams for each subcase (a–d) indicate the predicted segregation of the edited *ura3* and *ade2* alleles after two replications. The number of expected WT genotypes is depicted as # × WT. Plots show ARFs for target strand combinations for cases 1 and 2. All values represent mean ± SD for three replicates. p values from ordinary one-way ANOVA Dunnett's multiple comparisons test (alpha = 0.05). Comparisons are to WT (B) and WT-None (E). \*p < 0.05; \*\*p < 0.005; \*\*\*p ≤ 0.001; \*\*\*\*p ≤ 0.0001. See also Figure S1.



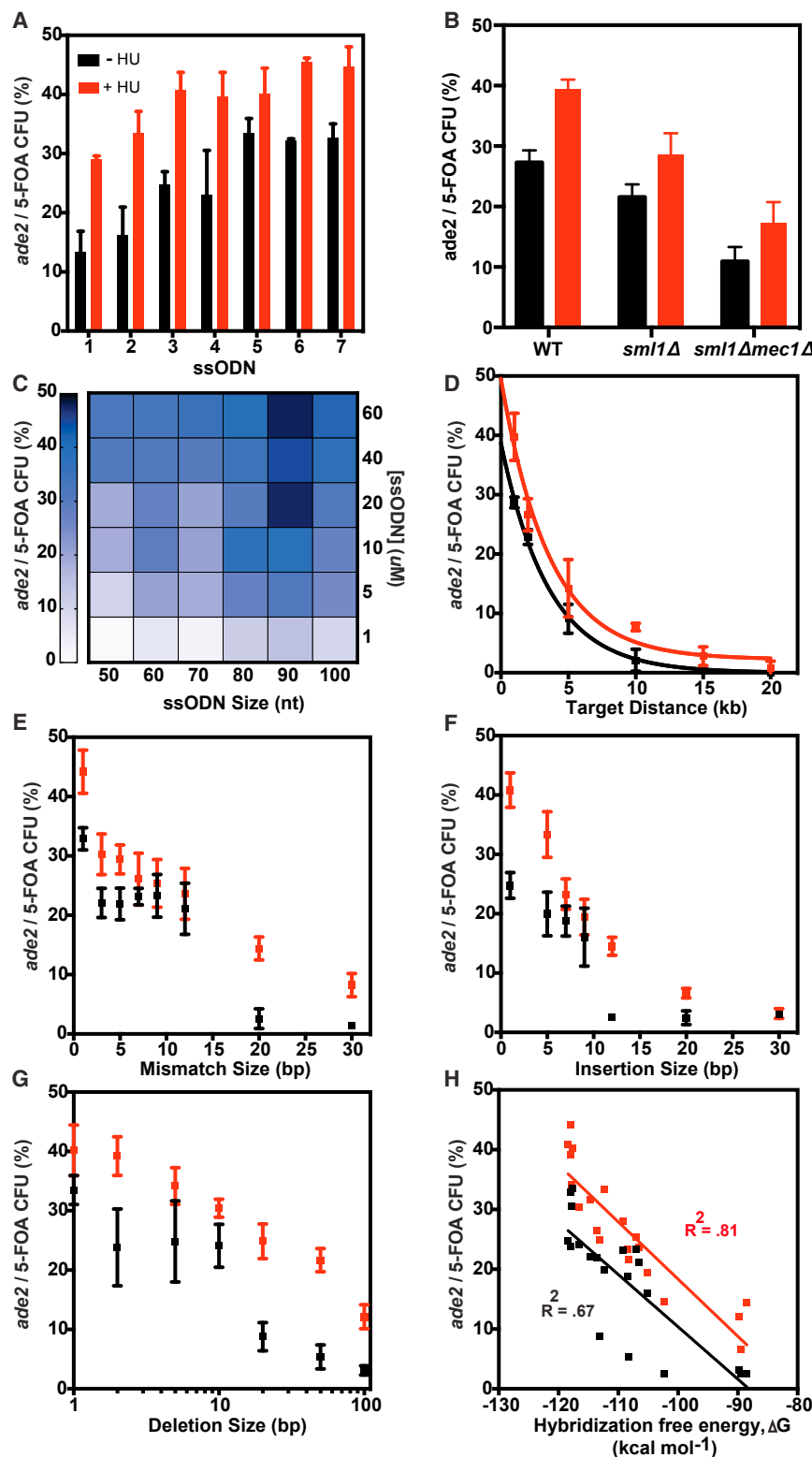


**Figure 2. Investigating Replication Dynamics for Incorporation of Diverse Mutations with ssODNs**

(A) The effect of hydroxyurea (HU) treatment (red) on seven ssODNs each containing a single bp change.

(B) Effect of Mec1 deletion  $\pm$  HU.

(C) Optimization of ssODN concentration and size for *ura3 + ade2* ssODNs. Heatmap shows mean ARF for each ssODN. See Figure S2G for these data as mean  $\pm$  SD.

(D) ARFs for increasing target site distances from the *URA3* marker. Non-linear curve fit one-phase decay equation:  $Y = (Y_0 - Z) \times \exp(-K \times X) + Z$ ; (+HU:  $Y_0 = 49.6$ ,  $Z = 2.25$ ,  $K = 0.279$ ), (-HU:  $Y_0 = 38.7$ ,  $Z = 2.22 \times 10^{-16}$ ,  $K = 0.2826$ ).

(E-G) ARFs of various genome modifications at a 1.5-kb distance in *ADE2*: mismatches (E), insertions (F), and deletions (G).

(H) The hybridization-free energy plotted against the mean ARFs for all ssODNs tested in (E)-(G) with Pearson correlation coefficients.

Values in (A), (B), and (D)-(G) represent mean  $\pm$  SD for three replicates.

See also Figure S2.

targeting, we observed an optimum number of *ade2* mutants per 5-FOA CFU (ARF = 47.5%) using a 90 nt ssODN at 20  $\mu$ M (Figures 2C and S1G), and used these parameters for all subsequent experiments.

Since yeast origins are  $\sim$ 30 kb apart, we tested the effect of target distance for loci at increasing distances from the *Ori-URA3* locus (Figure 2D). ARFs decreased with target distance from the *Ori-URA3* locus, but remained  $>1\%$  at a distance of 20 kb. This decrease in ARF could be due to interference of replication from distal origins and warrants future investigation. To investigate the introduction of diverse mutations, we tested a set of ssODNs containing a contiguous block of mismatches, insertions, or deletions within *ADE2* ( $\sim$ 1.5 kb from the *Ori-URA3*) for the *msh2 $\Delta$*  strain. The ARF was inversely correlated to the number of bp targeted for modification, in which a single bp mismatch, insertion, or deletion was incorporated with an ARF  $>40\%$  (Figures 2E–2G). Mismatches up to 30 bp and deletions up to 100 bp were incorporated at  $\sim$ 10% efficiency (Figures 2E and 2G). Insertions are the least efficient modification with ARFs  $\leq 10\%$  for insertions  $>12$  bps (Figure 2F). The two-state hybridization free energy between the ssODN and genomic target sequence was a better predictor of ARFs for ssODNs tested in the +HU condition than –HU (Figure 2H) (Markham and Zuker, 2008). These data demonstrate that ssODN annealing at the replication fork is enhanced in close proximity to the *Ori-URA3* locus and can generate diverse mutations required for precision genome editing.

### Generation of Precise Combinatorial Genome Modifications via Multiplexing and Cycling

Since the average size of Okazaki fragments in *S. cerevisiae* ( $\sim$ 165 nt) (Smith and Whitehouse, 2012) is significantly shorter than that of *E. coli* ( $\sim$ 1–2 kb) (Wu et al., 1992), we hypothesized that the introduction of multiple ssODNs at high density at the replication fork could enable a high degree of multiplex gene editing. To test this hypothesis, we targeted 10 loci across the *ADE2* gene in WT and *msh2 $\Delta$*  strains (Figure 3A). The mean number of ssODNs incorporated per clone was higher in *msh2 $\Delta$*  (2.2 per clone) than WT (1.2 per clone). We hypothesized that HU would enhance ssODN multiplexing and tested ssODN pools targeting 2, 4, 6, and 10 sites across the *ADE2* gene (Figure 3A). For 10-target multiplexing, HU increased the mean number of ssODNs incorporated in *msh2 $\Delta$*  to 3.4 per clone, whereas WT exhibited no multiplex enhancement with HU (Figure S3A). The mean number of ssODNs incorporated plateaued at  $\sim$ 1 mutation per clone for WT and increased as a function of the number of target loci for *msh2 $\Delta$*  (Figure 3A). We observed clones with diverse combinations of targeted changes for all multiplex pools (Figure S3A).

To increase genetic diversity, we developed a strategy for continuous diversification of a yeast cell population by cyclical introduction of a complex pool of ssODNs coupled to  $\pm$  *URA3* selections (Figure 3B; see the STAR Methods for details). We designed a set of 10 ssODNs containing 5 degenerate (“N”) insertion positions spaced 10bp apart in each ssODN. We analyzed 100 *ade2* clones by Sanger sequencing after each cycle, and observed a broad distribution of *ade2* genotypes (Figures 3C–3E; Table S3), ranging from one to five insertions per

ssODN. After three cycles of eMAGE with the same pool of *ade2* ssODNs, the maximum number of mutations increased from 37 to 42 per clone and the average number of mutations increased from 14.4 to 20.4 per clone (Figure 3D). The average number of ssODNs incorporated increased from 5.1 to 6.0 ssODNs per clone (Figure 3E). All of the sequenced clones contained unique genotypes in cycles 1 and 2, and 76% were unique in cycle 3. We performed whole-genome sequencing (WGS) for 12 clones from each cycle in order to understand the effect of the eMAGE protocol on the background mutation rate. Consistent with the reported rate for *msh2 $\Delta$*  ( $7.1 \times 10^{-8}$  mutations per bp per generation) (Lang et al., 2013), we observed a mean mutation rate of  $8.1 \times 10^{-8}$  mutations per bp per generation (Figures S4A–S4C; Tables S3, S4, and S5). These data demonstrate the ability to rapidly create combinatorial genomic diversity by iterative incorporation of a complex pool of ssODNs at the replication fork.

### High-Throughput Sequencing of a Diversified Population

To measure the genetic diversity created by eMAGE and to further study multiplex ssODN incorporation, we performed high-throughput sequencing (HTS) of a diversified population at a defined region of *ADE2* (Figure 4). We transformed a pool of three ssODNs each encoding five degenerate insertions at *ADE2* to an initial population of  $\sim$  $10^8$  cells, expecting  $\sim$  $10^5$  edited cells to survive 5-FOA liquid selection (Figure 4A; see Figure S2F for *URA3* selection efficiencies). The 15 insertion positions span a 307 bp region of *ADE2* such that the sequence diversity could be analyzed with  $2 \times 250$  bp paired-end reads. Using a computational pipeline, we observed  $\sim$  $1.59 \times 10^5$  and  $\sim$  $6.70 \times 10^5$  unique variants for read quality scores of Q30 and Q20, respectively (Figures 4B and S4D–S4F). The mutants contained one, two, or three ssODNs incorporated, and the two most abundant contained either the most proximal ssODN (ssODN 1) or all three ssODNs (Figure 4C). For the mutants with two ssODNs incorporated, we did not observe a strong preference for adjacent ssODN pairs. We performed a rarefaction analysis and the sequence accumulation plots (Figures 4D and S4F) did not plateau before the number of HTS reads reached its maximum (Amiram et al., 2015; Szpiech et al., 2008). Given this result, we hypothesize that our diversity estimates likely represent lower bounds and expect that the actual complexity can be quantified as HTS technologies improve.

Consistent with our Sanger sequencing data (Figures S3B and S3C), we observed a distribution of insertions per ssODN with a 3' position bias (Figures 4E and 4F). Prior work (Rodriguez et al., 2012) implicated the Fen1-endonuclease in flap degradation at the 5' end of ssODNs. We posited that this effect could be partially explained by truncated ssODNs arising from errors in DNA synthesis since ssODNs are synthesized 3' to 5'. Although we observed a reduction in 3' bias with a PAGE purified ssODN (Figure S3D), this effect was not completely eliminated with PAGE purification, suggesting that the effect could be a combination of truncated ssODNs from synthesis and native processing. The greater read-depth with HTS allowed us to uncover additional processing events at the 3', potentially due to proof-reading activity of DNA polymerase  $\delta$  (Anand et al., 2017), and,

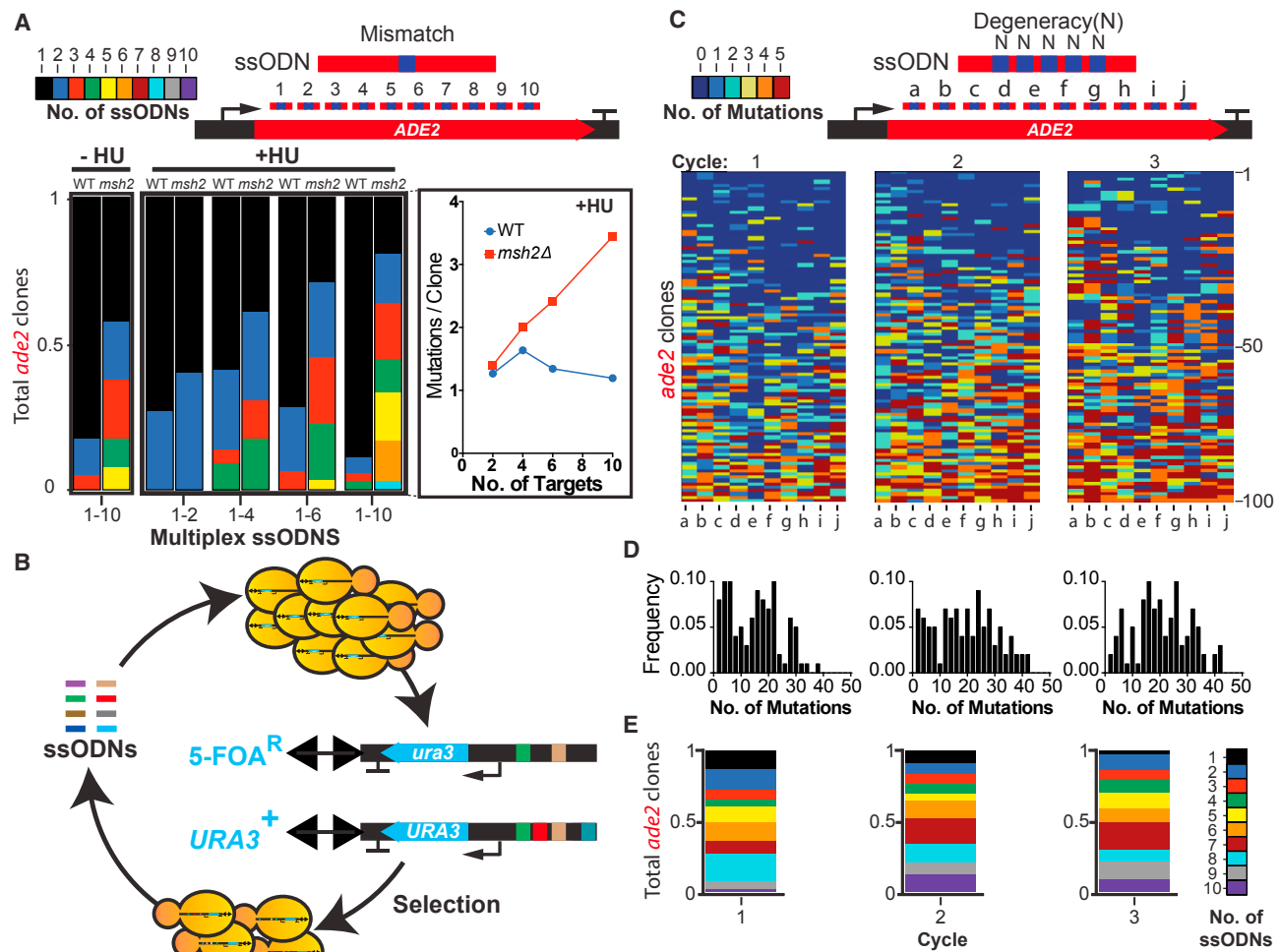


**Figure 3. Multiplex ssODN Incorporation and Cycling**

(A) Multiplexed ssODNs harboring single point mutations across *ADE2*. Pools of 2-, 4-, 6-, and 10-plex ssODNs with HU; 10 ssODNs untreated (–HU). Panel shows *msh2Δ* compared to WT mean mutations per clone for +HU. Number of clones sequenced (n), n = 20 (2-plex), n = 22 (4-plex), n = 32 (6-plex), n = 36 (10-plex), and n = 40 (10-plex –HU condition).

(B) Iterative cycling of ssODNs to a population of cells. *URA3* is targeted by an “OFF” ssODN in odd cycles and an “ON” ssODN in even cycles. Positive-negative selections enable recovery of diversified chromosomes.

(C) Cyclical introduction of 10-plex ssODNs containing 5 degenerate “N” positions per ssODN. Heatmaps show sequence data for n = 100 *ade2* mutant clones per cycle. ssODN position (columns a–j) and clonal sequence data (rows 1–100).

(D) Frequency distributions of *ade2* bp mutations per clone for each cycle.

(E) Number of ssODNs incorporated per *ade2* clone for each cycle.

See also Figure S3 and Table S3.

in some cases, we observed clones lacking an internal mutation in the ssODN but retaining the 5' and 3' mutations (Figures 4G–4I).

### Targeted Diversification of a Heterologous Biosynthetic Pathway

To further study our ability to generate multisite combinatorial genomic variation at bp-level precision, we targeted a heterologous  $\beta$ -carotene pathway for the creation of diverse variants. The pathway consists of four constitutively expressed genes (*crtE*, *crtI*, *crtYB*, and *tHMG1*), which convert farnesyl diphosphate (FPP) to  $\beta$ -carotene through a series of enzymatic steps in

*S. cerevisiae* (Figure 5A) (Mitchell et al., 2015). We designed a pool of ssODNs to precisely target distinct genetic elements in promoters, open reading frames (ORFs), and terminators (Figures 5B and 5C; Table S4; see the STAR Methods for details of ssODN designs). Overall, the ssODN pool consisted of 74 ssODNs encoding targeted mutations at 482 nucleotide positions.

After a single eMAGE cycle with the entire 74 ssODN pool, we observed clones with diverse colorimetric phenotypes that differed from both the ancestral strain and the full set of 15 possible combinatorial pathway gene KOs (Figures 5D and S5A). We selected diverse variants for Sanger sequencing and high-performance liquid chromatography (HPLC) analysis to



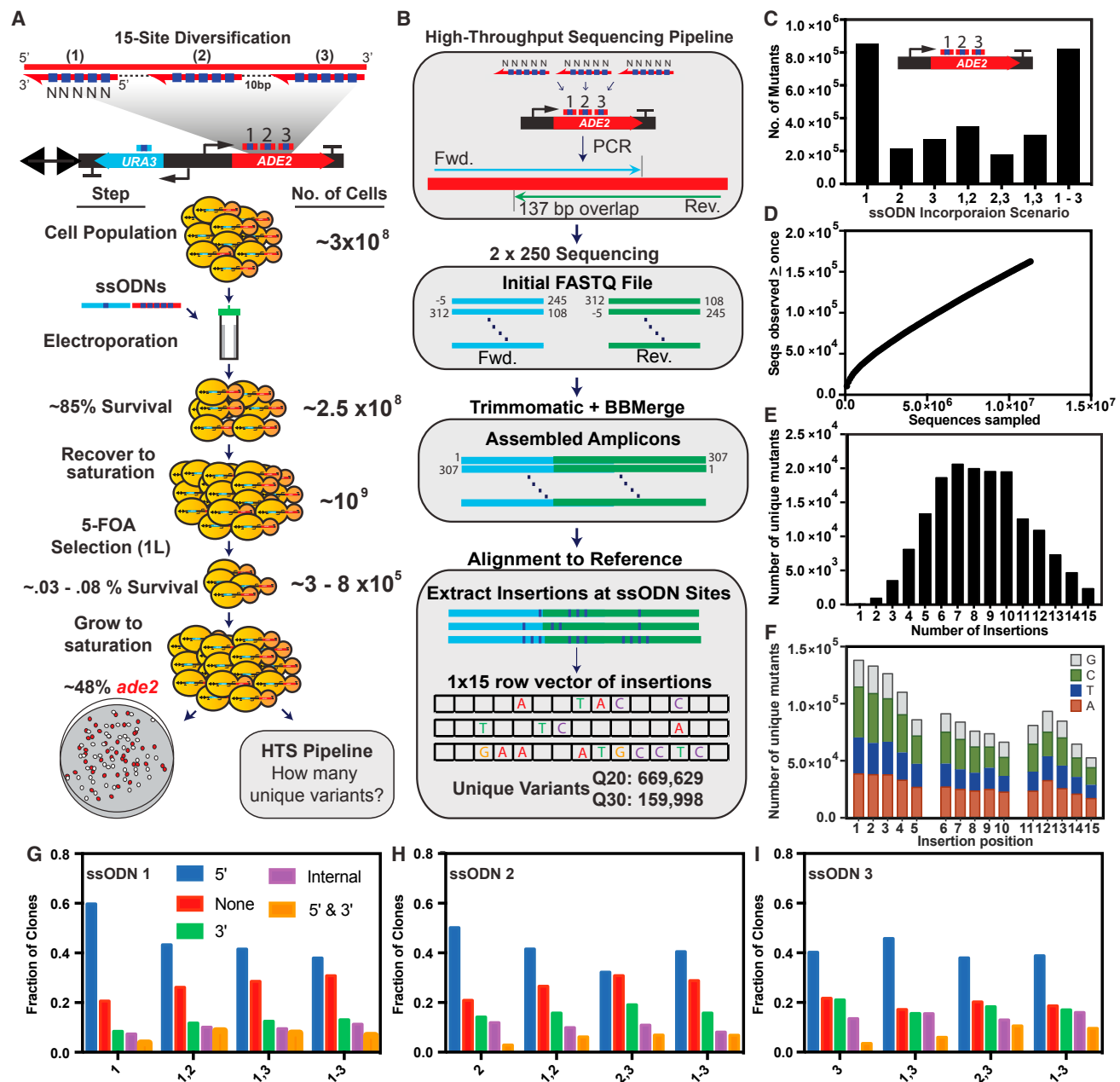


**Figure 4. Deep-Sequencing Analysis of a Population Diversified by eMAGE**

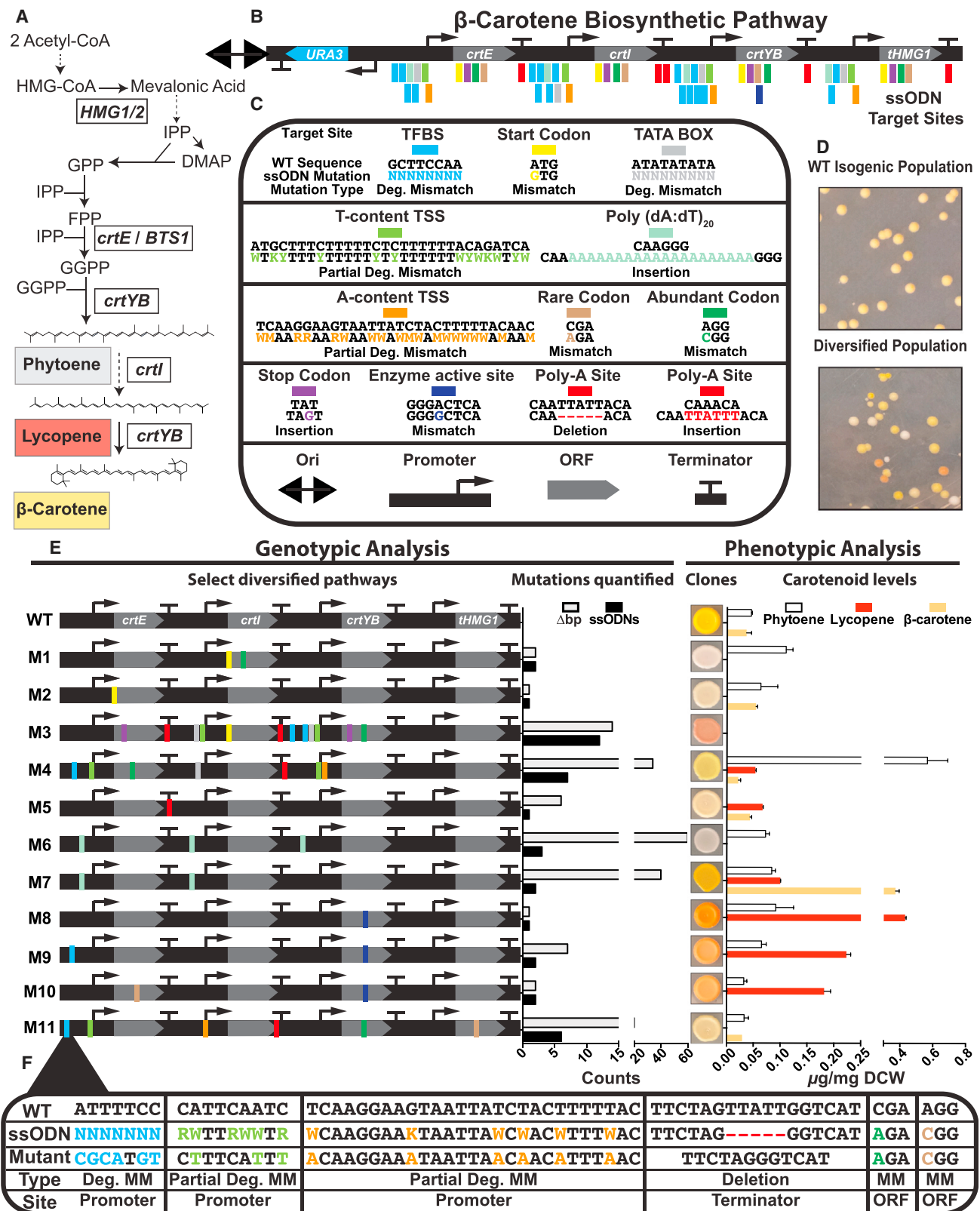
(A) 15-site diversification of the *ADE2* gene with three ssODNs containing five degenerate (N) positions each. A population of cells is diversified via electroporation of the ssODN pool and *ura3* selection ssODN. After recovery to saturation, the population is subjected to liquid selection in 5-FOA media and grown to saturation; a small aliquot is plated to YPD; and a genomic prep is processed by the HTS pipeline.

(B) Pipeline for determining the number of unique variants generated by eMAGE. A PCR amplicon containing the diversified locus is deep sequenced using 2 × 250 sequencing. The overlapping paired-end reads are trimmed and processed for quality score and aligned to the reference genome. The ssODN insertions are extracted and analyzed to quantify the total number of unique mutants.

(C–F) Plots derived from Q30 sequence data. Abundance of mutants detected with each possible ssODN incorporation scenario (C). Rarefaction curve illustrating the accumulation of sequences seen at least once as a function of the total number of sequences observed (D). Number of targeted insertions present in unique mutant sequences (E). Positional distribution of the targeted insertions with the relative abundance of each nucleotide at each ssODN (F).

(G–I) Plots show the frequency and type of processing events for ssODN 1 (G), ssODN 2 (H), and ssODN 3 (I) in all incorporation scenarios. Colored bars represent the removal of an insertion mutation at the 5' portion of the ssODN (blue), 3' (green), both 5' and 3' (orange), at an internal position in the ssODN sequence with retained 5' and 3' insertions (purple), and incorporation of all five insertions (red).

See also Figure S4 and Tables S4 and S5.



(legend on next page)

reveal causal genotype-phenotype relationships. The analyzed clones contained a range of 1–60 bp changes and 1–12 ssODNs incorporated (Figures 5E, S6, and S7). Consistent with our findings for the *ADE2* locus, we observed enhanced ARFs for targets more proximal to *URA3* and targets with the fewest bp changes (Figure S7). We observed many examples of precise genetic modifications that resulted in distinct phenotypic variation. For example, three clones with varied carotenoid levels contained mutations in the *crtE* gene element distinct from the *crtE* KO (KO1): an alternative start codon (M2), polyadenylation signal site insertion (M5), and a rare codon (M35). KO of *crtI* (KO2) resulted in buildup of phytoene corresponding to a white phenotype, which was indistinguishable from a clone containing an alternate start and an abundant arginine codon in *crtI* (M1). In contrast, a deletion of 6 bp in the *crtI* terminator (M39) resulted in  $\beta$ -carotene buildup and no detectable phytoene. Incorporation of nucleosome disfavoring poly(dT)<sub>20</sub> sequences in promoters for *crtE* and *crtI* resulted in  $\sim 7$ -fold increase in  $\beta$ -carotene production (M7), whereas an additional poly(dT)<sub>20</sub> in the promoter of *crtYB* led to detection of phytoene only (M6). We also recovered high lycopene variants containing *crtYB*-D52G and additional gene modifications that altered lycopene levels (M8–M10 and M12–M14). Notably, clone M11 contained 22 bp of targeted mutations derived from 6 distinct ssODNs in all three classes of genetic elements across all four genes (Figures 5E and 5F). The background mutation rate ( $6.6 \times 10^{-8}$  mutations per bp per generation) for 55 diversified clones measured by WGS was consistent with prior findings (Figures S4G–S4I). Since the  $\beta$ -carotene pathway contains four promoters and three terminators found at native loci in the genome, we also checked for ssODN incorporation at these off-target sites and did not observe any ssODN-derived mutations (Tables S4 and S5). These results demonstrate the ability to sample phenotypic variation through precise bp editing at target sites, which could be applied to any set of genetic elements to elucidate causal links between genotype and phenotype.

We then tested whether targeted edits in genes located on different chromosomes could be generated across haploids in parallel and combined via mating. We constructed a *MAT $\alpha$*  haploid containing the *crtE* gene adjacent to a *URA3* cassette at Ori ARS510 on chromosome 5 and a *MATa* haploid containing the *crtI*, *crtYB*, and *thMG1* genes at Ori ARS1516 on chromosome 15 (Figures 6A–6C). Upon mating, the resultant diploids showed the yellow phenotype indicative of the presence of all four genes of the WT  $\beta$ -carotene pathway (Figure 6D). Next, we generated parallel diversity of the haploids with ssODN pools targeting the genes present in each strain, and mated the popu-

lations to generate diploid strains with diversified phenotypes resulting from the independent chromosomes targeted (Figure 6E). We repeated the process for *crtE* at Ori ARS446 on chromosome 4 and Ori ARS702 on chromosome 7 and observed equivalent results (Figure S5C). These experiments demonstrate the generalizability of replication fork targeting of distinct loci on multiple chromosomes (4, 5, 7, and 15) and subsequent mating of the diversified haploid strains to amplify combinatorial genetic variation in diploids.

### Altering Transcriptional Logic with ssODNs

Finally, we tested whether ssODNs can be used to precisely replace transcription factor binding sites (TFBS) to alter regulatory logic. We designed a set of ssODNs to replace native TFBS in the  $\beta$ -carotene pathway with the 18 bp galactose-inducible Gal4 binding sequence (Figure 7A). We transformed cells with the Gal4 ssODNs and an ssODN containing the *crtYB*-D52G mutation to enhance the detection of new phenotypes. We isolated clones with altered color phenotypes on glucose versus galactose plates and sequenced the targeted loci. Consistent with previous data (Figures 2D and 2E), at  $\sim 1.5$  kb we observed the insertion of Gal4 TFBS with ARFs between 8%–22% and ARFs  $< 5\%$  at distances  $> 3$  kb (Figure 7B). We studied five clones that exhibited color changes when spotted to galactose to confirm the introduction of a Gal4 TFBS (G1–G5) (Figure 7C). RT-qPCR of these clones confirmed that genes with a Gal4 TFBS were induced on galactose and are responsible for the color changes (Figure 7D; Table S7). For example, G4 showed the strongest galactose gene induction of *crtI* (1130%). We observed galactose induction of some genes that did not contain a Gal4 TFBS (G4 and G5), which could be due to altered transcription levels of genes in the pathway. Similar to the native *GAL1* gene, induction of *crtI* expression in G4 was dose responsive to a range (0.01%–5%) of galactose (Figure 7E). These data show that eMAGE can introduce sequence elements that can impart galactose-based induction of gene expression capable of altering transcriptional levels. This strategy can be applied to many other transcriptional logic elements (e.g., TetR-tetO) and promoters to create diverse sets of genetic pathways with programmable regulatory properties.

### DISCUSSION

In this study, we developed a eukaryotic genome engineering technology by elucidating a new mechanism that avoids the creation of DSBs by precise annealing of ssODNs at the DNA replication fork to enact bp precision and combinatorial genome

#### Figure 5. Targeted Diversification of a $\beta$ -Carotene Pathway

- (A)  $\beta$ -carotene biosynthetic pathway constitutively expressed in yeast.  
 (B) The genomically integrated  $\beta$ -carotene pathway adjacent to *Ori-URA3*. ssODN target sites in promoters, ORFs, and terminators.  
 (C) Examples of specific mutations for each sequence element targeted. Degenerate mutations abbreviated as “deg.” and mismatch as “MM.” N, mixed bases A, T, G, C; W, mixed bases A, T; Y, mixed bases C, T; R, mixed bases A, G; K, mixed bases G, T; M, mixed bases A, C.  
 (D) Images showing representative colonies expressing the  $\beta$ -carotene biosynthetic pathway (WT) and diversified phenotypes after eMAGE.  
 (E) Genotypic and phenotypic analysis of select clones containing diversified genotypes and phenotypes uncovered with Sanger sequencing and HPLC analysis. Total number of ssODNs incorporated (black bar) and number of targeted bp changes (light-gray bar). HPLC data for clonal production of  $\beta$ -carotene (orange), lycopene (red), and phytoene (white) (micrograms per milligrams dry cell weight). Values represent mean  $\pm$  SD for three replicates.  
 (F) Expanded view of clone M11 containing targeted edits in promoters, ORFs, and a terminator.  
 See also Figures S5, S6, and S7 and Table S6.

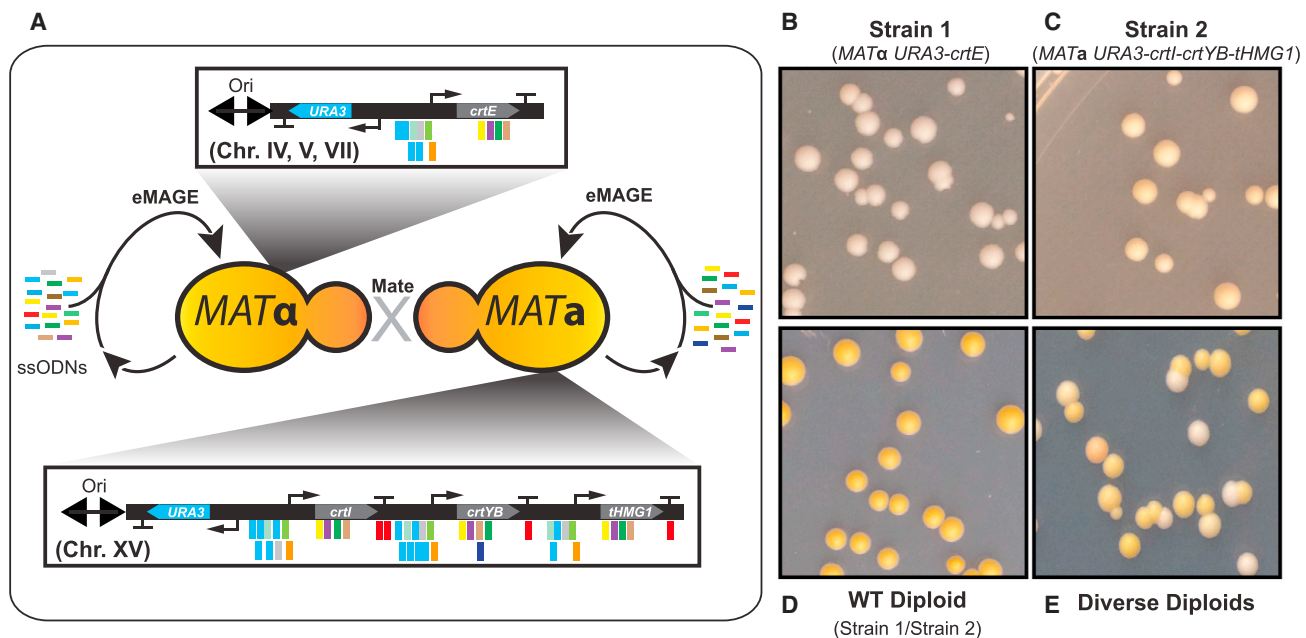


**Figure 6. Genomic Diversification across Chromosomes and Combined through Mating**

(A) Parallel diversification of the  $\beta$ -carotene pathway split into two haploid strains. *URA3-crtE* is integrated in three *MAT $\alpha$*  strains at chromosomes (chr) 4, 5, or 7 to demonstrate eMAGE targeting on additional chr. *URA3-crtI-crtYB-thmG1* is integrated at chr 15 in *MATa*. After performing eMAGE on the strains in parallel, the populations are combined with mating to yield diversified diploids.

(B) Strain 1 genotype is *MAT $\alpha$  ARS510-URA3-crtE* at chr 5.

(C) Strain 2 genotype is *MATa ARS1516 URA3-crtI-crtYB-thmG1* at chr 15.

(D) Control mating of strains 1 and 2 shows ancestral phenotype of full pathway.

(E) Mating of diversified populations shows altered phenotypes in diploids.

See also Figure S5.

editing across many genetic loci. Incorporation of ssODNs at the replication fork is independent of Rad51, and overexpression of Rad51 reduces ARF potentially by competing for ssODN binding (Song and Sung, 2000). In recent work, Rad51-independent HDR has also been reported for CRISPR-Cas9 (Collonier et al., 2017). Rad52 and Rad59 are involved in Rad51-independent processing of Okazaki fragments (Lee et al., 2014), and the loss of detectable ARFs in *rad59 $\Delta$*  and *rad52 $\Delta$ rad59 $\Delta$*  compared to the neutral effect of its paralog (*rad52 $\Delta$* ) suggests a unique role for Rad59 to promote annealing of ssODNs at the replication fork. Although Rad52 may contribute to ssODN annealing at the replication fork, it also mediates loading of Rad51 to RPA-bound ssDNA (Song and Sung, 2000), whereas Rad59 does not contain a known Rad51 binding domain (Erler et al., 2009). The rescue of *rad59 $\Delta$*  and *rad52 $\Delta$ rad59 $\Delta$*  by Rad52, Rad59, and  $\lambda$  Red Beta suggests that an ssDNA annealing function is required for the high ARFs we observed in this study and supports our model of ssODN annealing at the replication fork. We did not observe further enhancement of *rad51 $\Delta$*  with overexpression of SSAPs, which suggests that the replication fork annealing pathway is nearly saturated in *rad51 $\Delta$* . The partial rescue of *rad59 $\Delta$*  by Rad51 matched the ARF of Rad51 overexpression in WT, suggesting that these are Rad51-mediated HR events. Surprisingly, Rad51 also partially rescued ARF in *rad52 $\Delta$ rad59 $\Delta$*  despite the absence of its mediator Rad52. Thus, Rad51 might exhibit low-level HR or replication fork annealing activity in *rad52 $\Delta$ rad59 $\Delta$* .

Our results reveal several factors that govern ARFs. First, selection for ssODN incorporation at the replication fork enriches for a competent subpopulation. Second, combining the selectable ssODN with a pool of ssODNs targeting proximal loci permits kinetically driven incorporation of ssODNs within the same replication fork in contrast to loci separated on different chromosomes. Third, when the selection marker and target loci reside on the same side of an active Ori, targeting ssODNs to the lagging strand is optimal; if they reside on opposite sides of the Ori then targeting cosegregating strands is favorable. Fourth, slowing replication fork speed with HU increases multiplex genome editing at downstream loci. Fifth, the ARF decrease in *sml1 $\Delta$ mec1 $\Delta$*  suggests that Mec1-dependent signaling partially stabilizes the replication fork (Branzei and Foiani, 2010) during ssODN incorporation. Sixth, unlike HU, UV exposure does not amplify ARFs, suggesting that ssODN incorporation at the replication fork is not mediated by a UV-induced DNA damage response. Further insights into the ssODN annealing mechanism through studies of Rad59, additional HR factors (e.g., Rad54, Rad55, Rad57, and Dmc1), SSAPs, DNA replication or repair gene combinations, and modulation of replication fork kinetics could enhance eMAGE.

For single-site editing, we observed similar ARFs in WT and *msh2 $\Delta$*  strains; however, our data show that MMR inhibits multiplex gene editing and therefore decreases the generation of genome complexity across the population. Although MMR

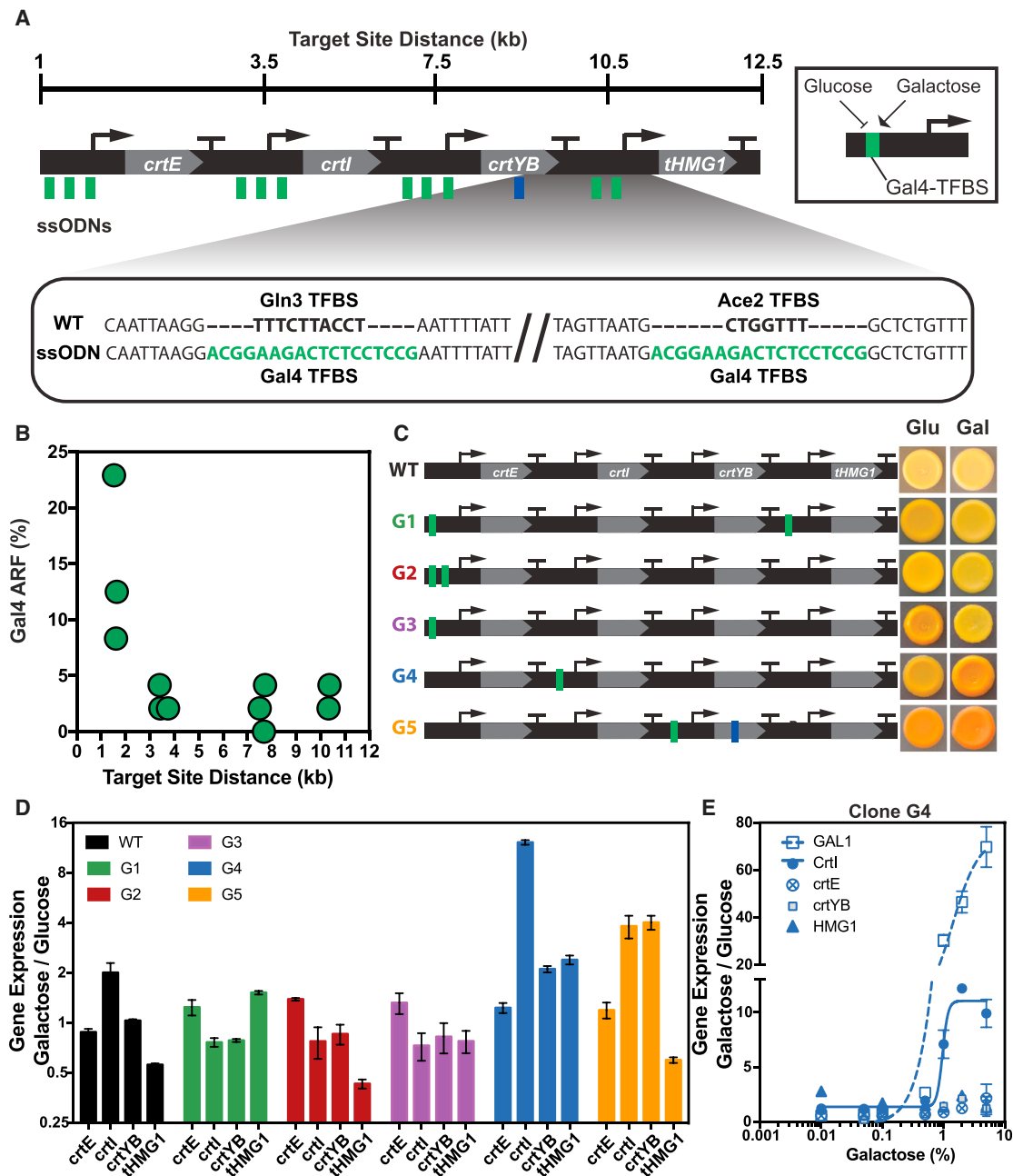


**Figure 7. Introduction of Gal4 Transcriptional Logic Sequences with ssODNs**

(A) ssODNs containing the 18-nt Gal4 (green) binding site targeted to replace native TFBS (bold) in promoters and a ssODN containing *crtYB*-D52G mutation (blue) at distances between 1 and 11 kb across the pathway.

(B) Plot shows observed ARF for each Gal4 ssODN at the indicated distance.  $n = 48$  sequenced clones.

(C) Mutant pathways containing Gal4 TFBS inserted in promoters and clonal spots show phenotypes of the clones on glucose (Glu) and galactose (Gal).

(D) Fold change in gene expression in galactose versus glucose.

(E) Fold change in gene expression of clone G4 across a range of galactose at the native *GAL1* gene and the engineered pathway. Non-linear curve fit for *GAL1* and *crtI*.  $R^2 = 0.97$  (*GAL1*) and  $0.96$  (*crtI*).

Values in (D) and (E) represent mean  $\pm$  SD for three replicates.

See also Table S7.



mutants are not desirable when trying to maintain genome stability, we envision directed evolution and pathway engineering applications, as shown here, that could benefit from an elevated mutation rate. Alternatively, transient disabling of MMR through small-molecule inhibitors, dominant-negative mutants, RNAi, or CRISPRi approaches could be used to introduce genetic modifications during a transient relaxed genomic state (disabled MMR) followed by rapid return to a stabilized genomic state (intact MMR).

Although the goal of our study does not aim to maximize titers of small molecule production, our approach to diversify the  $\beta$ -carotene pathway can serve as a blueprint for natural product discovery to investigate and activate cryptic biosynthetic gene clusters or metabolic engineering applications to produce high-value molecules from heterologous genetic sources (Krivoruchko and Nielsen, 2015). Current methods to tune the expression of biosynthetic pathways in yeast rely on the use of promoter swapping strategies (Mitchell et al., 2015; Wingler and Cornish, 2011). Although these approaches are effective, the possible modes of gene expression are limited to quantal units of transcription dictated by the promoter library. Diversification of biosynthetic pathways with eMAGE enables targeting across all associated genetic elements and allows for exploration of greater diversity. In contrast to  $\sim 10^2$  variants constructed using current DNA synthesis technologies (Smanski et al., 2014), generating targeted and complex ( $>10^5$ ) diversity across multiple genetic loci is uniquely enabled by eMAGE. An equivalent diversification of the  $\beta$ -carotene pathway would not be possible using DSB methods, in which  $\sim 41$  DSBs are required to target 482 nucleotides and many of the single bp mutations would not sufficiently prevent re-cutting by the DSB machinery. Given prior reports (Jakočiūnas et al., 2015), we expect that  $>4$  DSBs would be lethal, and thus intractable with DSB-mediated genome editing technologies. Since CRISPR-Cas9 can efficiently introduce large genetic fragments into the genome and eMAGE can enact many precise combinatorial edits, we envision that the two approaches could be used in concert to recombine and diversify pathways.

Eukaryotic MAGE uniquely enables the construction of targeted sets of genetic variants that can be functionally studied to elucidate causal links between genotype and phenotype. The eMAGE process could be automated, employed to uncover new allelic interactions to complement synthetic genetic arrays (Costanzo et al., 2016), and used to hierarchically construct highly modified chimeric genomes from multiple strains. We anticipate that eMAGE capabilities could be included in future synthetic eukaryotic chromosome projects (Annaluru et al., 2014; Boeke et al., 2016) to enable efficient single-bp precision editing of designer genomes. Finally, the approach used for *S. cerevisiae* targets conserved mechanisms and establishes a framework for developing efficient multiplex ssODN annealing methods in multicellular eukaryotes, including plants and animals.

## STAR★METHODS

Detailed methods are provided in the online version of this paper and include the following:

- KEY RESOURCES TABLE
- CONTACT FOR REAGENT AND RESOURCE SHARING

## ● EXPERIMENTAL MODEL AND SUBJECT DETAILS

### ● METHOD DETAILS

- Strain Construction
- Media
- Plasmid Assembly for overexpression of HR Genes and SSAPs
- Yeast ssODN Electroporation with Rad51-Dependent HR
- ssODN transformations for eMAGE
- UV Irradiation
- Target Distance Efficiency Determination
- Multiplex Incorporation of ssODNs and Cycling
- Whole genome sequencing sample prep
- Generation of mutant population for HTS diversity analysis
- HTS diversity sample preparation and sequencing
- Design of ssODNs for  $\beta$ -carotene Pathway Diversification
- HPLC Characterization of Carotenoids
- Isolation of RNA and RT-qPCR Conditions

### ● QUANTIFICATION AND STATISTICAL ANALYSES

- Statistical Notes
- Calculation of ARF
- Calculation of ssODN hybridization free energies
- Unique Mutants from Multiplex Incorporation of ssODNs and Cycling
- Whole genome sequencing read filtering, mapping, and variant calling
- HTS diversity filtering and processing of paired end reads into merged sequences
- HTS diversity computational analysis
- Determination of Primer Efficiency for RT-qPCR Analysis
- Measurement of Relative Gene Expression with RT-qPCR

### ● DATA AND SOFTWARE AVAILABILITY

## SUPPLEMENTAL INFORMATION

Supplemental Information includes seven figures and seven tables and can be found with this article online at <https://doi.org/10.1016/j.cell.2017.10.034>.

## AUTHOR CONTRIBUTIONS

F.J.I. and E.M.B. conceived the study, designed the experiments, and wrote the manuscript. E.M.B. performed the experiments with assistance from B.O.A.-O., P.M., and C.M.Y. P.M. performed the HTS analysis.

## ACKNOWLEDGMENTS

We thank P. Sung, S. Dellaporta, M. Hochstrasser, T. Xu, and J. Rinehart; the anonymous reviewers; and members of the Isaacs Lab for valuable feedback. We thank G.S. Roeder for generous access to lab and reagents. E.M.B. is funded by NSF-GRFP (1122492) and an NIH Predoctoral Training Grant in Genetics (T32GM007499). C.M.Y. was funded by the Howard Hughes Medical Institute. F.J.I. gratefully acknowledges support from DARPA (HR0011-15-C-0091 and N66001-12-C-4020), DOE (DE-FG02-02ER63445), NIH (1R01GM117230-01 and 1U54CA209992-01), and the Arnold and Mabel Beckman Foundation. E.M.B. and F.J.I. have filed a provisional application with the US Patent and Trademark Office on this work. F.J.I. is a founder of enEvolv.

Received: October 27, 2016  
Revised: August 29, 2017  
Accepted: October 19, 2017  
Published: November 16, 2017

## REFERENCES

- Amiram, M., Haimovich, A.D., Fan, C., Wang, Y.S., Aerni, H.R., Ntai, I., Moonan, D.W., Ma, N.J., Rovner, A.J., Hong, S.H., et al. (2015). Evolution of translation machinery in recoded bacteria enables multi-site incorporation of nonstandard amino acids. *Nat. Biotechnol.* **33**, 1272–1279.
- Anand, R., Beach, A., Li, K., and Haber, J. (2017). Rad51-mediated double-strand break repair and mismatch correction of divergent substrates. *Nature* **544**, 377–380.
- Annaluru, N., Muller, H., Mitchell, L.A., Ramalingam, S., Stracquadanio, G., Richardson, S.M., Dymond, J.S., Kuang, Z., Scheifele, L.Z., Cooper, E.M., et al. (2014). Total synthesis of a functional designer eukaryotic chromosome. *Science* **344**, 55–58.
- Boeke, J.D., Church, G., Hessel, A., Kelley, N.J., Arkin, A., Cai, Y., Carlson, R., Chakravarti, A., Cornish, V.W., Holt, L., et al. (2016). The genome project-write. *Science* **353**, 126–127.
- Bolger, A.M., Lohse, M., and Usadel, B. (2014). Trimmomatic: a flexible trimmer for Illumina sequence data. *Bioinformatics* **30**, 2114–2120.
- Brachmann, C.B., Davies, A., Cost, G.J., Caputo, E., Li, J., Hieter, P., and Boeke, J.D. (1998). Designer deletion strains derived from *Saccharomyces cerevisiae* S288C: a useful set of strains and plasmids for PCR-mediated gene disruption and other applications. *Yeast* **14**, 115–132.
- Branzei, D., and Foiani, M. (2010). Maintaining genome stability at the replication fork. *Nat. Rev. Mol. Cell Biol.* **11**, 208–219.
- Carr, P.A., Wang, H.H., Sterling, B., Isaacs, F.J., Lajoie, M.J., Xu, G., Church, G.M., and Jacobson, J.M. (2012). Enhanced multiplex genome engineering through co-operative oligonucleotide co-selection. *Nucleic Acids Res.* **40**, e132.
- Chandrasegaran, S., and Carroll, D. (2016). Origins of programmable nucleases for genome engineering. *J. Mol. Biol.* **428** (5 Pt B), 963–989.
- Collonnier, C., Epert, A., Mara, K., Maciot, F., Guyon-Debast, A., Charlot, F., White, C., Schaefer, D.G., and Nogu  , F. (2017). CRISPR-Cas9-mediated efficient directed mutagenesis and RAD51-dependent and RAD51-independent gene targeting in the moss *Physcomitrella patens*. *Plant Biotechnol. J.* **15**, 122–131.
- Cong, L., Ran, F.A., Cox, D., Lin, S., Barretto, R., Habib, N., Hsu, P.D., Wu, X., Jiang, W., Marraffini, L.A., and Zhang, F. (2013). Multiplex genome engineering using CRISPR/Cas systems. *Science* **339**, 819–823.
- Costantino, N., and Court, D.L. (2003). Enhanced levels of lambda red-mediated recombinants in mismatch repair mutants. *Proc. Natl. Acad. Sci. USA* **100**, 15748–15753.
- Costanzo, M., VanderSluis, B., Koch, E.N., Baryshnikova, A., Pons, C., Tan, G., Wang, W., Usaj, M., Hanchard, J., Lee, S.D., et al. (2016). A global genetic interaction network maps a wiring diagram of cellular function. *Science* **353**, 353.
- Detloff, P., Sieber, J., and Petes, T.D. (1991). Repair of specific base pair mismatches formed during meiotic recombination in the yeast *Saccharomyces cerevisiae*. *Mol. Cell Biol.* **11**, 737–745.
- DiCarlo, J.E., Conley, A.J., Penttil  , M., J  ntti, J., Wang, H.H., and Church, G.M. (2013). Yeast oligo-mediated genome engineering (YOGI). *ACS Synth. Biol.* **2**, 741–749.
- Doudna, J.A., and Charpentier, E. (2014). Genome editing. The new frontier of genome engineering with CRISPR-Cas9. *Science* **346**, 1258096.
- Erl  r, A., Wegmann, S., Elie-Caille, C., Bradshaw, C.R., Maresca, M., Seidel, R., Habermann, B., Muller, D.J., and Stewart, A.F. (2009). Conformational adaptability of Redbeta during DNA annealing and implications for its structural relationship with Rad52. *J. Mol. Biol.* **391**, 586–598.
- Farzadfard, F., Perli, S.D., and Lu, T.K. (2013). Tunable and multifunctional eukaryotic transcription factors based on CRISPR/Cas. *ACS Synth. Biol.* **2**, 604–613.
- Friedman, K.L., Brewer, B.J., and Fangman, W.L. (1997). Replication profile of *Saccharomyces cerevisiae* chromosome VI. *Genes Cells* **2**, 667–678.
- Fu, Y., Foden, J.A., Khayter, C., Maeder, M.L., Reyon, D., Joung, J.K., and Sander, J.D. (2013). High-frequency off-target mutagenesis induced by CRISPR-Cas nucleases in human cells. *Nat. Biotechnol.* **31**, 822–826.
- Gibson, D.G. (2011). Enzymatic assembly of overlapping DNA fragments. *Methods Enzymol.* **498**, 349–361.
- Gietz, R.D. (2014). Yeast transformation by the LiAc/SS carrier DNA/PEG method. *Methods Mol. Biol.* **1205**, 1–12.
- Horwitz, A.A., Walter, J.M., Schubert, M.G., Kung, S.H., Hawkins, K., Platt, D.M., Hernday, A.D., Mahatdejkul-Meadows, T., Szeto, W., Chandran, S.S., and Newman, J.D. (2015). Efficient multiplexed integration of synergistic alleles and metabolic pathways in yeasts via CRISPR-Cas. *Cell Syst.* **1**, 88–96.
- Inui, M., Miyado, M., Igarashi, M., Tamano, M., Kubo, A., Yamashita, S., Asahara, H., Fukami, M., and Takada, S. (2014). Rapid generation of mouse models with defined point mutations by the CRISPR/Cas9 system. *Sci. Rep.* **4**, 5396.
- Jakob  ciunas, T., Bonde, I., Herrg  rd, M., Harrison, S.J., Kristensen, M., Pedersen, L.E., Jensen, M.K., and Keasling, J.D. (2015). Multiplex metabolic pathway engineering using CRISPR/Cas9 in *Saccharomyces cerevisiae*. *Metab. Eng.* **28**, 213–222.
- Jinek, M., Chylinski, K., Fonfara, I., Hauer, M., Doudna, J.A., and Charpentier, E. (2012). A programmable dual-RNA-guided DNA endonuclease in adaptive bacterial immunity. *Science* **337**, 816–821.
- Komor, A.C., Kim, Y.B., Packer, M.S., Zuris, J.A., and Liu, D.R. (2016). Programmable editing of a target base in genomic DNA without double-stranded DNA cleavage. *Nature* **533**, 420–424.
- Kow, Y.W., Bao, G., Reeves, J.W., Jinks-Robertson, S., and Crouse, G.F. (2007). Oligonucleotide transformation of yeast reveals mismatch repair complexes to be differentially active on DNA replication strands. *Proc. Natl. Acad. Sci. USA* **104**, 11352–11357.
- Krivoruchko, A., and Nielsen, J. (2015). Production of natural products through metabolic engineering of *Saccharomyces cerevisiae*. *Curr. Opin. Biotechnol.* **35**, 7–15.
- Lajoie, M.J., Rovner, A.J., Goodman, D.B., Aerni, H.R., Haimovich, A.D., Kuznetsov, G., Mercer, J.A., Wang, H.H., Carr, P.A., Mosberg, J.A., et al. (2013). Genomically recoded organisms expand biological functions. *Science* **342**, 357–360.
- Lang, G.I., Parsons, L., and Gammie, A.E. (2013). Mutation rates, spectra, and genome-wide distribution of spontaneous mutations in mismatch repair deficient yeast. *G3 (Bethesda)* **3**, 1453–1465.
- Lee, M., Lee, C.H., Demin, A.A., Munashingha, P.R., Amangyeld, T., Kwon, B., Formosa, T., and Seo, Y.S. (2014). Rad52/Rad59-dependent recombination as a means to rectify faulty Okazaki fragment processing. *J. Biol. Chem.* **289**, 15064–15079.
- Li, H. (2013). Aligning sequence reads, clone sequences and assembly contigs with BWA-MEM. *arXiv*, arXiv:13033997v1 [q-bio.GN], <https://arxiv.org/abs/1303.3997>.
- Liu, L., Maguire, K.K., and Kmiec, E.B. (2004). Genetic re-engineering of *Saccharomyces cerevisiae* RAD51 leads to a significant increase in the frequency of gene repair in vivo. *Nucleic Acids Res.* **32**, 2093–2101.
- Lubliner, S., Keren, L., and Segal, E. (2013). Sequence features of yeast and human core promoters that are predictive of maximal promoter activity. *Nucleic Acids Res.* **41**, 5569–5581.
- Mali, P., Yang, L., Esvelt, K.M., Aach, J., Guell, M., DiCarlo, J.E., Norville, J.E., and Church, G.M. (2013). RNA-guided human genome engineering via Cas9. *Science* **339**, 823–826.
- Markham, N.R., and Zuker, M. (2008). UNAFold: software for nucleic acid folding and hybridization. *Methods Mol. Biol.* **453**, 3–31.

- Mitchell, L.A., Chuang, J., Agmon, N., Khunsriraksakul, C., Phillips, N.A., Cai, Y., Truong, D.M., Veerakumar, A., Wang, Y., Mayorga, M., et al. (2015). Versatile genetic assembly system (VEGAS) to assemble pathways for expression in *S. cerevisiae*. *Nucleic Acids Res.* 43, 6620–6630.
- Paquet, D., Kwart, D., Chen, A., Sproul, A., Jacob, S., Teo, S., Olsen, K.M., Gregg, A., Noggle, S., and Tessier-Lavigne, M. (2016). Efficient introduction of specific homozygous and heterozygous mutations using CRISPR/Cas9. *Nature* 533, 125–129.
- Rivera-Torres, N., and Kmiec, E.B. (2016). Genetic spell-checking: gene editing using single-stranded DNA oligonucleotides. *Plant Biotechnol. J.* 14, 463–470.
- Rodriguez, G.P., Song, J.B., and Crouse, G.F. (2012). Transformation with oligonucleotides creating clustered changes in the yeast genome. *PLoS ONE* 7, e42905.
- San Filippo, J., Sung, P., and Klein, H. (2008). Mechanism of eukaryotic homologous recombination. *Annu. Rev. Biochem.* 77, 229–257.
- Schmittgen, T.D., and Livak, K.J. (2008). Analyzing real-time PCR data by the comparative C(T) method. *Nat. Protoc.* 3, 1101–1108.
- Smanski, M.J., Bhatia, S., Zhao, D., Park, Y., BA Woodruff, L., Giannoukos, G., Ciulla, D., Busby, M., Calderon, J., Nicol, R., et al. (2014). Functional optimization of gene clusters by combinatorial design and assembly. *Nat. Biotechnol.* 32, 1241–1249.
- Smith, D.J., and Whitehouse, I. (2012). Intrinsic coupling of lagging-strand synthesis to chromatin assembly. *Nature* 483, 434–438.
- Song, B., and Sung, P. (2000). Functional interactions among yeast Rad51 recombinase, Rad52 mediator, and replication protein A in DNA strand exchange. *J. Biol. Chem.* 275, 15895–15904.
- Storici, F., and Resnick, M.A. (2003). Delitto perfetto targeted mutagenesis in yeast with oligonucleotides. *Genet. Eng. (N. Y.)* 25, 189–207.
- Sung, P. (1997). Function of yeast Rad52 protein as a mediator between replication protein A and the Rad51 recombinase. *J. Biol. Chem.* 272, 28194–28197.
- Szpiech, Z.A., Jakobsson, M., and Rosenberg, N.A. (2008). ADZE: a rarefaction approach for counting alleles private to combinations of populations. *Bioinformatics* 24, 2498–2504.
- Tsai, S.Q., and Joung, J.K. (2016). Defining and improving the genome-wide specificities of CRISPR-Cas9 nucleases. *Nat. Rev. Genet.* 17, 300–312.
- Van der Auwera, G.A., Carneiro, M.O., Hartl, C., Poplin, R., Del Angel, G., Levy-Moonshine, A., Jordan, T., Shakir, K., Roazen, D., Thibault, J., et al. (2013). From FastQ data to high confidence variant calls: the Genome Analysis Toolkit best practices pipeline. *Curr. Protoc. Bioinformatics* 43, 11.10.1–11.10.33.
- Wang, H.H., Isaacs, F.J., Carr, P.A., Sun, Z.Z., Xu, G., Forest, C.R., and Church, G.M. (2009). Programming cells by multiplex genome engineering and accelerated evolution. *Nature* 460, 894–898.
- Wingler, L.M., and Cornish, V.W. (2011). Reiterative recombination for the in vivo assembly of libraries of multigene pathways. *Proc. Natl. Acad. Sci. USA* 108, 15135–15140.
- Winzeler, E.A., Shoemaker, D.D., Astromoff, A., Liang, H., Anderson, K., Andre, B., Bangham, R., Benito, R., Boeke, J.D., Bussey, H., et al. (1999). Functional characterization of the *S. cerevisiae* genome by gene deletion and parallel analysis. *Science* 285, 901–906.
- Wu, C.A., Zechner, E.L., and Mariani, K.J. (1992). Coordinated leading- and lagging-strand synthesis at the *Escherichia coli* DNA replication fork. I. Multiple effectors act to modulate Okazaki fragment size. *J. Biol. Chem.* 267, 4030–4044.
- Xie, W., Lv, X., Ye, L., Zhou, P., and Yu, H. (2015). Construction of lycopene-overproducing *Saccharomyces cerevisiae* by combining directed evolution and metabolic engineering. *Metab. Eng.* 30, 69–78.
- Xu, W., Aparicio, J.G., Aparicio, O.M., and Tavaré, S. (2006). Genome-wide mapping of ORC and Mcm2p binding sites on tiling arrays and identification of essential ARS consensus sequences in *S. cerevisiae*. *BMC Genomics* 7, 276.
- Yamamoto, T., Moerschell, R.P., Wakem, L.P., Ferguson, D., and Sherman, F. (1992). Parameters affecting the frequencies of transformation and co-transformation with synthetic oligonucleotides in yeast. *Yeast* 8, 935–948.
- Yang, L., Güell, M., Niu, D., George, H., Lesha, E., Grishin, D., Aach, J., Shrock, E., Xu, W., Poci, J., et al. (2015). Genome-wide inactivation of porcine endogenous retroviruses (PERVs). *Science* 350, 1101–1104.
- Zhang, G.C., Kong, I.I., Kim, H., Liu, J.J., Cate, J.H., and Jin, Y.S. (2014). Construction of a quadruple auxotrophic mutant of an industrial polyploid *saccharomyces cerevisiae* strain by using RNA-guided Cas9 nuclease. *Appl. Environ. Microbiol.* 80, 7694–7701.

## STAR★METHODS

### KEY RESOURCES TABLE

REAGENT or RESOURCE	SOURCE	IDENTIFIER
Chemicals, Peptides, and Recombinant Proteins		
Dithiothreitol (DTT)	AmericanBio	Cat# 30653
Hydroxyurea (HU)	MP	Cat# 210202325
5-Fluoroorotic acid (5-FOA)	Research Products International	Cat# F10501-10.0
Hygromycin B	Invitrogen	Cat# 31282-04-9
RAD51 inhibitor (RI-1)	Abcam	Cat# ab144558
$\beta$ -carotene analytical standard	Santa Cruz Biotech	Cat# sc-202485
Phytoene analytical standard	CaroteNature	Cat# CN-0044
Lycopene analytical standard	Santa Cruz Biotech	Cat# 502-65-8
Zymolyase-100T	MP	Cat# 32093
Critical Commercial Assays		
Luna One Step Universal RT-qPCR kit	NEB	Cat# E3005
RNeasy Kit	QIAGEN	Cat# 74104
TruSeq DNA PCR-Free HT Kit	Illumina	Cat# FC-121-3003
DNeasy Blood & Tissue Kit	QIAGEN	Cat# 69504
Deposited Data		
Whole-genome sequencing raw reads <a href="#">Figure S4</a> and <a href="#">Tables S3, S4, and S5</a>	GenBank SRA	BioProject ID: PRJNA413161 BioSample accession # SAMN07737501–SAMN07737596
Deep sequencing raw reads <a href="#">Figures 4 and S4</a>	GenBank SRA	BioProject ID: PRJNA413161 BioSample accession # SAMN07737500
Experimental Models: Organisms/Strains		
<i>S. cerevisiae</i> Strains - See <a href="#">Table S1</a>	This paper; Indicated strains were purchased from Open Biosystems.	N/A
Oligonucleotides		
ssODNs, see <a href="#">Tables S2 and S6</a>	This paper, ssODNs purchased from IDT	N/A
Recombinant DNA		
Plasmid Source for PCR product: Beta Carotene Pathway	<a href="#">Mitchell et al., 2015</a>	pJC178
Plasmid: Cas9-NAT	<a href="#">Zhang et al., 2014</a>	Addgene #64329
Plasmid: pRPR1_gRNA_handle_RPR1	<a href="#">Farzadfard et al., 2013</a>	Addgene #49014
Software and Algorithms		
Trimmomatic	<a href="#">Bolger et al., 2014</a>	<a href="http://www.usadellab.org/cms/?page=trimmomatic">http://www.usadellab.org/cms/?page=trimmomatic</a>
BWA-mem	<a href="#">Li, 2013</a>	<a href="http://bio-bwa.sourceforge.net/">http://bio-bwa.sourceforge.net/</a>
Picard Tools	Broad Institute	<a href="https://github.com/broadinstitute/picard">https://github.com/broadinstitute/picard</a>
BBMerge	Bbmap	<a href="https://sourceforge.net/projects/bbmap/">sourceforge.net/projects/bbmap/</a>
RealignerTargetCreator and IndelRealigner	Broad Institute	<a href="https://software.broadinstitute.org/gatk/documentation/tooldocs/current/org_broadinstitute_gatk_tools_walkers_indels_RealignerTargetCreator.php">https://software.broadinstitute.org/gatk/documentation/tooldocs/current/org_broadinstitute_gatk_tools_walkers_indels_RealignerTargetCreator.php</a>
UNAFold	<a href="#">Markham and Zuker, 2008</a>	<a href="http://unafold.rna.albany.edu/?q=DINAMelt/Two-state-melting">http://unafold.rna.albany.edu/?q=DINAMelt/Two-state-melting</a>
Prism 7	GraphPad	<a href="https://www.graphpad.com/scientific-software/prism/">https://www.graphpad.com/scientific-software/prism/</a>

## CONTACT FOR REAGENT AND RESOURCE SHARING

Further information and requests for resources and reagents should be directed to and will be fulfilled by the Lead Contact, Farren Isaacs ([farren.isaacs@yale.edu](mailto:farren.isaacs@yale.edu)).

## EXPERIMENTAL MODEL AND SUBJECT DETAILS

A complete list of *Saccharomyces cerevisiae* strains used in this study can be found in [Table S1](#). Strain BY4741 (*MATa his3Δ1 leu2Δ0 met15Δ0 ura3Δ0*) was chosen due to its common use as a laboratory strain and for its use in the *Saccharomyces* Genome Deletion Project ([Brachmann et al., 1998](#); [Winzeler et al., 1999](#)). MMR KO strains from the *Saccharomyces* Genome Deletion Project were purchased (Open Biosystems, Thermo Scientific).

## METHOD DETAILS

### Strain Construction

Strains harboring the *URA3* marker for coupled ssODN selection (eMAGE) were constructed via standard homologous recombination with a dsDNA *URA3* PCR product containing 60nt of overlap to the genomic locus followed by selection on CSM-Uracil plates. For Case-I the following primers were used to amplify and integrate *URA3*. Forward primer with ADE2 locus overlap: 5'-ATAA TATTGTCCATTAGTTCTTAATAAAAGGTCAGCAAGAGTCAATCACTTAGTATTACGATGTAGAAAAGGATTAAAGATGCTAAGAGAT AGTGA-3' Reverse primer with ARS1516 locus overlap: 5'-TTAATTATGATACATTTCTTACGTCATGATTGATTATTACAGCTATGCT GACAAATGACTCAATGCGTCCATCTTTACAGTCCTG-3'.

For Case-II, Forward primer: 5'- TCCATCTGACATTACTATTTTGCATTTTAATTTAATTAGAACTTGACTAGCGCACTACCAGATG TAGAAAAGGATTAAAGATGCTAAGAGATAGTGA-3'. Reverse primer: 5'- TGAAGTTTCTTTTATAATAACCTGGTCAAAAGCTTTCAA TATATAATACATTTGGTATTTCATGCGTCCATCTTTACAGTCCTG-3'. The β-carotene pathway is derived from *Xanthophyllomyces dendrorhous* and was amplified by PCR from plasmid pJC178 ([Mitchell et al., 2015](#)), then genomically incorporated at ARS1516 or at the indicated ARS location for mating experiments ([Figures 5, 6, S5, S6, and S7](#); [Table S1](#)). The β-carotene pathway PCR product was genomically integrated using a CRISPR-Cas9 genome integration. First, the WT strain BY4741 was transformed with a constitutive expression Cas9-NAT plasmid, a gift from Yong-Su Jin (Addgene #64329) ([Zhang et al., 2014](#)) by standard PEG/Lithium acetate transformation ([Gietz, 2014](#)) and positive clones were selected via Nourseothricin (clonNat) selection. Second, the gRNA plasmid, pRPR1\_gRNA\_handle\_RPR1t, a gift from Timothy Lu, (Addgene #49014) ([Farzadfar et al., 2013](#)) containing gRNA target site sequence 'CTTGTTCATGGCTACGAAC' located at chrXV:566360 was transformed along with the β-carotene pathway PCR product. Positive clones were selected using leucine auxotrophic selection, inspection for yellow colored phenotype, and sequencing confirmation. Third, the *URA3* selection marker was introduced between the ARS1516 and β-carotene pathway in the Case-I orientation as described above with sequence overlap to the β-carotene pathway. Fourth, *MSH2* was deleted using a dsDNA recombination of an *hphMX* cassette conferring hygromycin B resistance. All modified loci were sequence verified in the final strain EMB294 used in this study.

### Media

For general strain manipulation cells were grown in YPADU liquid medium, which consists of YPD (10 g/L Yeast Extract, 20 g/L Peptone, 20 g/L Dextrose), supplemented with 40mg/L adenine hemisulfate, and 40mg/L uracil. For *URA3*-coupled ssODN experiments (eMAGE), strains were grown in CSM-Ura medium during odd numbered cycles and CSM-Ura+5-FOA (1g/L) + uracil (50mg/L) medium during even numbered cycles. For HR gene overexpression experiments, *CEN/ARS* plasmids were maintained with the hygromycin B resistance marker. After electroporation, cells were allowed to recover in YPADU/0.5M Sorbitol (Recovery Medium).

### Plasmid Assembly for overexpression of HR Genes and SSAPs

To clone *pTEF1* expression plasmids for HR genes, all HR gene ORFs were PCR amplified from BY4741 genomic DNA prepared via a standard glass bead yeast genomic preparation protocol. The λ Red Beta gene was purchased as a dsDNA fragment (IDT) containing the SV40 nuclear localization sequence (NLS) at the N terminus. The Forward primers for each ORF contained 40 bases of 5' overhang with sequence identity to 3' end of the *TEF1* promoter. Reverse primers for each ORF contained 5' overhang with 40 bases of cyc1T terminator identity. Gibson assembly cloning ([Gibson, 2011](#)) was used to assemble a hygromycin B resistant (*hphMX*) *CEN/ARS* plasmid backbone (pRCVS6H) for each ORF to generate (pRCVS6H-pTEF1-ORF-CycT-hphMX plasmids). All plasmids were sequence verified.

### Yeast ssODN Electroporation with Rad51-Dependent HR

A 2mL culture was inoculated with a single colony and grown to saturation overnight in YPADU or YPADU + Hygromycin B (200μg/mL) for plasmid maintenance during HR overexpression experiments. The next day a 10mL culture was inoculated at OD<sub>600</sub> ~0.1 and grown for 6 hours in a roller drum at 30°C until OD<sub>600</sub> ~0.7-1.0 (~3x10<sup>7</sup> cells/mL). Cells were pelleted at 2,900x g for 3 minutes and washed twice with 40mL of room temperature dH<sub>2</sub>O. Cells were pre-treated with 1mL of TE pH 8 containing



500mM Lithium Acetate/25mM DTT (Pretreatment Buffer) for 30 minutes in the roller drum at 30°C. Cells were washed 1x with 1mL ice cold dH<sub>2</sub>O and 1x with 1mL ice cold 1M sorbitol. Cells were gently suspended in 200  $\mu$ L of 1M sorbitol + 2  $\mu$ M of total ssODN for each transformation, and added to a pre-chilled electroporation cuvette (0.2cm) on ice.  $\sim$ 2  $\mu$ M of ssODN was previously determined to be optimal for Rad51-dependent HR (DiCarlo et al., 2013). Electroporation was performed with the following parameters: 1500V, 25 $\mu$ F, 200 $\Omega$ . Immediately after pulsing, the cells were recovered in 6mL of Recovery Medium for 12 hours in the roller drum at 30°C.

### ssODN transformations for eMAGE

A list of ssODNs used for Figures 1, 2, 3, and 4 in this study can be found in Table S2 and for Figures 5, 6, and 7 the ssODNs can be found in Table S6. All ssODNs were designed as 90nt in length, with slight (1-3nt) length deviations for some ssODNs in an attempt to minimize secondary structure. For eMAGE experiments, a single colony was inoculated in 2mL CSM-Ura medium and grown overnight to saturation. The next day the culture was diluted 1:50 in 10mL of CSM-Ura and grown for 6 hours prior to electroporation. The ssODN concentration and size were determined from optimization experiments performed in Figure S2. A total of 20  $\mu$ M of 90nt ssODNs consisting of 50% selection ssODN 50% target ssODN(s) was used for eMAGE transformations. The optimal HU concentration was determined from Figure S2A and HU was used from Figures 2, 3, 4, 5, 6, and 7. The eMAGE pretreatment mixture contained 500mM HU in TE pH 8 / 500mM Lithium Acetate / 25mM DTT. Electroporation parameters for eMAGE were as described above. After 12 hours of recovery,  $\sim$ 10<sup>5</sup> cells were plated on 5-FOA selection plates for MMR mutant strains and  $\sim$ 10<sup>7</sup> cells were plated for strains with WT MMR. The resultant 5-FOA plates contained  $\sim$ 100-200 colonies which were subject to screening for target ssODN incorporation. The indicated ARF values represent mean  $\pm$  SD for three replicates unless otherwise indicated. For the Rad51 chemical inhibitor experiment (Figure S1I) the recovery medium was supplemented with inhibitor RI-1 (Abcam ab144558) + 1.5% DMSO for solubility and the untreated sample also contained 1.5% DMSO to control for any DMSO effects.

### UV Irradiation

UV irradiation was performed using a Stratalinker® UV crosslinker model 1800. After DTT treatment prior to the electroporation step, cells were washed and suspended in dH<sub>2</sub>O, irradiated with varying doses (0 - 10<sup>6</sup>  $\mu$ J) of UV, and immediately electroporated with ssODNs as described above.

### Target Distance Efficiency Determination

Target mutation distance is reported as the distance between the *URA3* marker mutation incorporated by the selection-ssODN and the mutation incorporated by the target-ssODN. For target distances of 1.5 and 2kb, ssODNs ade290RC and ade2\_Mult10 were used within the *ADE2* gene and the ARFs for these sites were determined by red/white phenotype screening. For targets at 5, 10, 15, and 20kb distances from the *Ori-URA3*, target sites were chosen that differ by only a single bp from an EcoRI restriction site. The target ssODN was designed to incorporate a bp change to create the EcoRI restriction site. For each target assayed, 96 clones were analyzed by colony PCR (ssODNs and Primers for the amplicons analyzed are listed in Table S2) coupled to EcoRI (NEB) digestion of the amplicon for 1hr at 37°C. The percentage of amplicons cut versus uncut is represented as the ARF for each distance site. Each distance experiment was performed in triplicate  $\pm$  HU treatment. ARF values represent mean  $\pm$  SD

### Multiplex Incorporation of ssODNs and Cycling

For multiplex eMAGE experiments targeting *ADE2*, red clones that grew on 5-FOA plates were assayed via yeast colony PCR and Sanger sequencing (Genewiz). Insertions were chosen for easy sequence detection since degenerate mismatches would contain WT sequence positions. For cycling experiments, cells were recovered in recovery media after electroporation as described above. After recovery in nonselective media, the population was subjected to liquid selection. For odd numbered cycles, the selection-ssODN creates a non-sense mutation in *ura3* for negative selection with 5-FOA, and the even cycle selection-ssODN restores the functional *URA3* gene for positive selection in uracil-dropout media. Selections were performed for 500 $\mu$ L of recovered culture seeded into 50mL of selection medium and grown to saturation at 30°C ( $\sim$ 2 days). After the first 1:100 selection the population was diluted 1:50 in selection media and grown for 6 hours for the next electroporation step. The process was repeated for 3 cycles. A total of 100 red clones were sequenced after each cycle.

### Whole genome sequencing sample prep

For each clone sequenced, 10mL of cell culture (OD<sub>600</sub> = 1) grown in YPADU was pelleted and treated with 100U of Zymolyase in buffer (1M Sorbitol in Tris pH = 7.4, 100mM EDTA, 14mM  $\beta$ -mercaptoethanol) for 90 minutes in a roller drum at 30°C. The resultant spheroplasts were used as the input for the DNeasy Blood & Tissue Kit (QIAGEN) to isolate genomic DNA for whole genome sequencing library preparation. 96 genomic libraries were prepped using the TruSeq DNA PCR-Free HT Kit (Illumina). The libraries were pooled and sequenced by the Yale Center for Genome Analysis using the Illumina HiSeq4000 with 2x100bp paired-end reads.

### Generation of mutant population for HTS diversity analysis

Approximately 3x10<sup>8</sup> cells were electroporated in a 20  $\mu$ M solution containing ssODNs designed to introduce at total of 15 insertions at *ADE2* targeted sites and the *ura3190* ssODN for selection. The three *ade2* ssODNs (Nade2MULTB, Nade2MULTC, and Nade2MULTD) each encode five insertions. After electroporation and recovery the entire population was then seeded in 1L of liquid

5-FOA selection media and grown to saturation over 2 days. 10mL of this selected population was used for the genome prep and 10  $\mu$ g or approximately  $5 \times 10^9$  genomic copies were seeded into the PCR reaction.

### HTS diversity sample preparation and sequencing

A 307-322 bp region (depending on the number of insertions introduced) including the bases targeted for mutagenesis was PCR amplified with primers that added five degenerate bps on each end. Forward primer: 5'-(N)(N)(N)(N)(N)TCCAATCCTCTTGATATC GAAAACTAGCTGA-3'; Reverse primer: 5'-(N)(N)(N)(N)(N)CATCGTATGCCAAAGTCCTCGACTTC-3'. The addition of degenerate bases aided in initial base calling during sequencing and reduced the need to add an increased fraction of phiX. The number of PCR cycles was limited to 12 in order to reduce the introduction of errors and bias. The PCR product was then gel purified and sent to the Yale Center for Genome Analysis for adaptor ligation and 2x250 paired-end sequencing on an Illumina HiSeq4000. This allowed for coverage of the entire amplicon and sufficient overlap between the paired-end reads to assemble phased sequences for each observed variant.

### Design of ssODNs for $\beta$ -carotene Pathway Diversification

See Table S6 for a complete list of ssODNs used to diversify the  $\beta$ -carotene pathway along with details regarding the specific mutation design and outcomes for each ssODN. We designed ssODNs to target known regulatory elements in promoters, ORFs, and terminators (Lubliner et al., 2013). For promoters, we targeted annotated transcription factor binding sites (TFBS), TATA boxes, insertion of nucleosome-disfavoring (dT)<sub>20</sub> sequences, and altered the A and T sequence content near the transcription start signal (TSS). Mutations to TFBS and TATA boxes were designed as 'N' degenerate and LOGO-inspired sequences to create the potential for both highly divergent sequences and single-bp changes. For each ORF, the ssODNs encoded an alternate start codon (GTG), a common codon, a rare codon, and a frameshift knockout (KO) mutation. In addition to mutations that alter gene expression, we also included a protein sequence change in the *crtYB* lycopene-cyclase domain known to increase lycopene production (Xie et al., 2015). Lastly, we targeted terminators at putative poly-A signal sites.

### HPLC Characterization of Carotenoids

Each of the analyzed clones was grown for 3 days at 30°C in 5mL YPADU media. Carotenoids were harvested from 1mL of cell culture. 1mL of cells was pelleted via centrifugation and washed twice with water. The resulting pellet was extracted with 200 $\mu$ L of hexane using glass bead disruption with the Beadbeater cell homogenizer (3x 45 s at 7,000rpm). After centrifugation, 120 $\mu$ L of the hexane carotenoid mixture was transferred to a glass vial and dried with a speedvac machine for 1 hour. The sample was then resuspended in 50/50 Hexane/Ethyl Acetate and filtered before HPLC analysis. 20 $\mu$ L of sample was injected for HPLC using an Agilent Poroshell 120 EC-C18 2.7  $\mu$ m 3.0  $\times$  50mm column. Peaks were detected using an isocratic elution with 50/50 Methanol/Acetonitrile (containing 0.1% Formic Acid). Analytical standards were used for quantification of  $\beta$ -carotene (detected at 475nm), phytoene (286nm), and lycopene (475nm). Carotenoid quantifications were calculated in relation to dry cell weight (DCW) for 100 $\mu$ L of cell culture dried for 2 days and weighed. Additional carotenoid peaks were observed beyond the three carotenoid peaks analyzed, which likely contribute to clone color in some cases. HPLC experiments were carried out as three replicates for all clones.

### Isolation of RNA and RT-qPCR Conditions

For RT-qPCR in Figure 7, three replicates of each clone were grown at 30°C in 5mL YP containing either 2% Galactose, 2% Dextrose, or a range of galactose (.01%–5%) for 16 hours. For galactose concentrations less than 2% (Figure 7D), the remainder of the carbon source was supplemented by addition of raffinose to a total of 2%. Total RNA was harvested from each sample using the RNeasy RNA isolation kit (QIAGEN) with an input of approximately  $3 \times 10^7$  cells (1mL of culture at OD<sub>600</sub> = 1). Total RNA was quantified using a Qubit fluorometer. Typical yield was approximately 200 ng/ $\mu$ L. For all samples a total of 10ng of RNA was used in each 20  $\mu$ L reaction. For RT-qPCR we used the Luna one-step universal RT-qPCR kit (NEB) run on a CFX Connect Real-Time System (Bio-Rad). The RT-qPCR reaction cycle consisted of the following steps: (1) 55°C for 10 min (2) 95°C for 1 min (3) 95°C for 10 s (4) 60°C for 30 s (5) Measure SYBR (6) Go to Step 3, 45X (7) Melt curve analysis 60°C to 95°C.

## QUANTIFICATION AND STATISTICAL ANALYSES

### Statistical Notes

For all statistical analysis and curve fitting of experimental samples we used Graphpad Prism 7 software. All datasets for Figures 1, 2, 5E (HPLC), 7D, and 7E (RT-qPCR) were carried out as three replicates. For Figures 1 and 2 each condition or strain was tested three independent times. For Figure 5E each clone was grown as three separate replicates, harvested as described, and the relevant pigments were measured by HPLC for each replicate. For Figures 7D and 7E each clone was grown as three independent replicates under each condition (glucose or galactose), RNA was harvested, and RT-qPCR was executed on each of the replicates. Where error bars are shown the data is reported as the Mean  $\pm$  SD. Statistical significance cutoff for all relevant experiments is \*  $p < 0.05$ . For all additional figures the number of samples 'n' is indicated in the figure caption.

### Calculation of ARF

The allelic replacement frequency (ARF) for homologous recombination of ssODNs at the *RPL28* gene (Figures 1B and S1A–S1F) was calculated by measuring the number of CFUs present on YPD-Cycloheximide agar plates divided by the number of CFUs present on YPD agar plates. When assaying for red *ade2* mutants without selection (Figure 1D) we plated  $\sim 10^3$  colonies on 10 YPD plates such that  $\sim 10^4$  colonies could be counted for each data point in the triplicate set. The ARF for single-plex *ura3* targeting (Figure S2F) was calculated by measuring the number of CFUs on CSM-uracil dropout plates divided by the number of CFUs on YPD plates. For all experiments where the ARF for *ade2* is reported, the ARF represents the number of *ade2* mutant (red) CFUs divided by the total number of 5-FOA resistant CFUs (or divided by YPD-Cycloheximide CFUs in Figures S1G and S1H; or divided by HIS3+ CFUs in Figure S2C). For Figure S1J the ARF for *ura3* after *rpl28* mutant selection was determined by first plating to YPD-Cycloheximide and then replica plating the surviving CFUs to 5-FOA plates. The ARF is the number of 5-FOA CFUs divided by the number of YPD-Cycloheximide CFUs. For all experiments the ARF are reported as a percent with the mean  $\pm$  SD shown.

### Calculation of ssODN hybridization free energies

Hybridization free energies were calculated for all ssODNs used in Figures 2E–2G using UNAFold two-state melting software available at <http://unafold.rna.albany.edu/?q=DINAMelt/Two-state-melting>. The following parameters were used: 30°C,  $[Na^+] = 1M$ ,  $[Mg^{2+}] = 0M$ , and strand concentration = 0.00001M. Each ssODN was hybridized the *ADE2* WT sequence. The Hybridization free energies were plotted against the mean ARF for each ssODN and analyzed with a linear regression using Graphpad Prism 7 and Pearson correlation coefficients are displayed in Figure 2H.

### Unique Mutants from Multiplex Incorporation of ssODNs and Cycling

For Figure 3C, in cycles 1 and 2 we observed 200 unique genotypes out of 200 sequenced, but for cycle 3 we observed 76 unique genotypes out of the 100 clones sequenced. Given that the degeneracy of the ssODN pool largely out-scales the number of clones assayed we would not expect any redundant genotypes to arise for independent clones in any cycle assayed. The 24 redundant clones observed in cycle 3 were comprised of 5 genotypes. These clones observed in cycle 3 are due to an enrichment of those genotypes that occurred from selection after cycle 2. For future experiments improved selection capabilities are necessary in order to ensure maintenance of high population diversity between multiple cycles. For the purposes of this small-scale demonstration the liquid selections we performed were seeded with 500uL of culture ( $\sim 10^3$ – $10^4$  edited genotypes) between each cycle. For applications requiring large library sizes, larger scale selections (Liters) could be employed to maintain the population complexity generated after electroporation.

### Whole genome sequencing read filtering, mapping, and variant calling

The sequencing reads generated for each sample were first filtered using Trimmomatic with the parameters “LEADING:3 TRAILING:3 SLIDINGWINDOW:2:30” in order to remove low quality bases at the ends of each read and to truncate reads containing consecutive bases with an average quality score below 30 (Bolger et al., 2014). The reads for each strain were then independently mapped to the current version of the S288C reference genome available at the *Saccharomyces* Genome Database using BWA-mem (Li, 2013). Reads were also mapped to a modified genome that incorporated the addition of the  $\beta$ -carotene pathway and KO of *MSH2*. Duplicates were marked in the resulting BAM file using Picard’s MarkDuplicates tool (<https://github.com/broadinstitute/picard>). The reads were then realigned using the RealignerTargetCreator and IndelRealigner tools from GATK (Van der Auwera et al., 2013). Variants were called using the GATK’s HaplotypeCaller with ploidy = 1 and when relevant with the -comp option in order to identify strain-specific variants by filtering out variants shared with the ancestor. The GATK tools SelectVariants and VariantFiltration were then used to filter SNP and Indel call sets and yield a final variant set.

### HTS diversity filtering and processing of paired end reads into merged sequences

The sequencing process generated 49,714,782 paired end reads. Trimmomatic was used to remove the first five degenerate bases added by the primers and trim reads with low quality bases. A sliding window requiring an average quality score of either Q20, Q25, or Q30 over two bases was used to trim the ends of lower quality reads. This resulted in 49,384,456, 48,711,289, and 47,505,196 paired end reads respectively passing quality control. BBMerge (<https://sourceforge.net/projects/bbmap/>) was then used to assemble the overlapping paired end reads into full-length amplicons. The “strict” stringency setting was used during this step. This resulted in 37,227,893, 24,116,204, and 12,065,464 fully assembled amplicons of which 16,704,731, 12,952,187, and 9,048,602 were WT length of 307 bp. Similar numbers of reads pass the quality trimming step at Q20 and Q30, but the number of assembled amplicons is dramatically different between the two cutoffs. This suggests that while a large number of reads are passing quality control at Q30 they are being trimmed to a greater extent and this is resulting in read pairs that no longer overlap and are unable to be assembled.

### HTS diversity computational analysis

The merged reads were then arranged in the same orientation and aligned to a WT copy of the edited genomic locus using the BWA-mem algorithm. Picard tools were used to calculate the experimental substitution error rate (<https://github.com/broadinstitute/picard>). Custom scripts then utilized the CIGAR and MD strings in the resulting SAM file to extract the position and base introduced

when insertions occurred at the targeted sites. Calculations of the distribution of the number of insertions introduced and the positional insertion distribution were then performed on these vectors containing the base introduced by each targeted insertion in an amplicon.

#### Determination of Primer Efficiency for RT-qPCR Analysis

Detailed information regarding the RT-qPCR parameters including primers and calculation of primer efficiencies are found in [Table S7](#). For determination of primer efficiencies we used purified total RNA from the EMB294 strain grown in glucose and galactose conditions. *ACT1* was used as a normalizing control gene, and primer pairs were designed for *crtE*, *crtI*, *crtYB*, and *tHMG1* ([Table S7](#)). Each primer pair was tested against a 10-fold dilution series of the RNA template from 100pg-100ng of total RNA in the RT-qPCR reaction and analyzed with a linear regression from a plot of log[RNA] versus  $C_q$ . The linear equations and  $R^2$  values for each primer pair in each condition are listed in [Table S7](#).

#### Measurement of Relative Gene Expression with RT-qPCR

For calculation of gene expression fold-change between glucose and galactose growth conditions we used the  $\Delta\Delta C_q$  method ([Schmittgen and Livak, 2008](#)) with *ACT1* as the normalizing gene. Reactions were performed using 10ng of total RNA, which is in the linear regime for the optimized conditions. GraphPad Prism 7 software was used for non-linear curve fitting for *GAL1* and *crtI* of clone G4 using a four-parameter variable-slope dose-response model.

#### DATA AND SOFTWARE AVAILABILITY

The accession number for the raw sequence reads from WGS ([Figure S4](#); [Tables S3](#), [S4](#), and [S5](#)) and deep sequencing ([Figures 4](#) and [S4](#)) experiments reported in this paper is SRA BioProject: PRJNA413161. The range of accession numbers for the WGS data reported in this paper is BioSample: SAMN07737501–SAMN07737596. The accession number for the deep sequencing reads reported in this paper is BioSample: SAMN07737500.

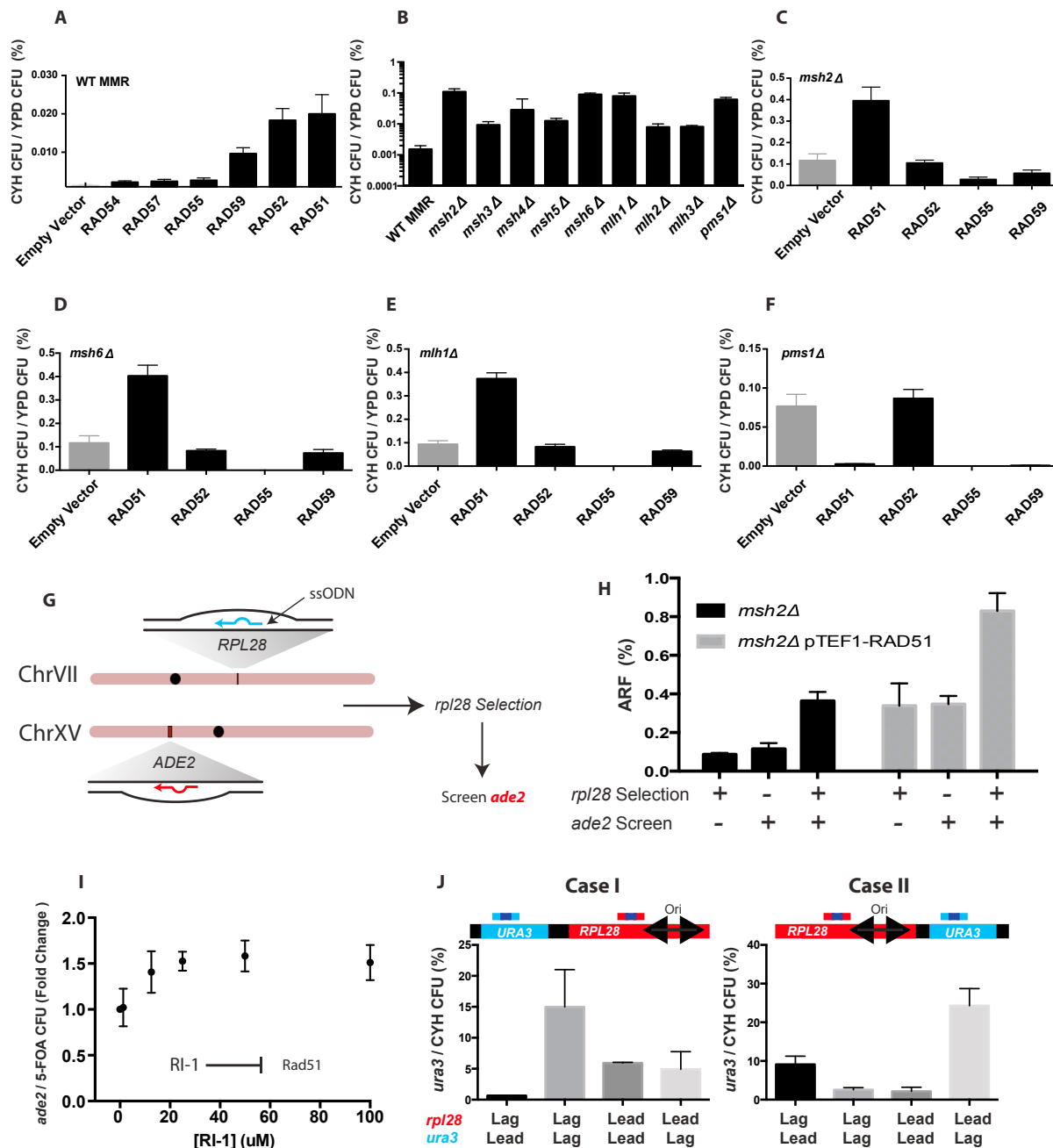


**Figure S1. Enhancement of ssODN Incorporation Efficiencies (ARF) through Constitutive Expression of HR Genes and Knockout of MMR, related to Figure 1**

(A–F) Measurement of *RPL28* ARF with overexpression of HR genes from *pTEF1* promoter with a *CEN/ARS* plasmid in BY4741 (WT) strain (A), mismatch repair (MMR) mutant strains (B), and combinations of *pTEF1*-HR gene overexpression with four MMR mutant strain backgrounds (C–F).

(G) Schematic illustrating co-transformation of two ssODNs targeted to loci on separate chromosomes to determine if the high ARFs (> 10%) observed for Ori-URA3-ADE2 require targeting within a contiguous chromosome. The ARF for ADE2 is measured before and after selection with cycloheximide.

(H) Measurement of ARF at *RPL28* (+,–), *ADE2* (–,–), and the ARF for *ADE2* after prior selection for *rpl28* mutants (+,+). Strains are *msh2* and *msh2 pTEF1-RAD51*.

(I) Dose-dependent fold-increase in *ADE2* mutants recovered with Rad51 inhibitor (RI-1) in YPADU 0.5M sorbitol + 1.5% DMSO, compared to vehicle control recovered in media containing only YPADU 0.5M sorbitol + 1.5% DMSO. Strain is EMB259.

(J) Additional mechanistic evidence for ssODN incorporation at replication forks. Strand targeting for marker-target orientation cases (I and II) at the *RPL28* locus. The *RPL28* gene contains an embedded origin of replication located at chromosome VII ~311600 (Xu et al., 2006), which enabled construction of Case-I and Case-II by placing *URA3* upstream or downstream of *RPL28*. The strand targeting efficiency (ARF %) trends are equivalent to those observed at the *ARS1516* locus. Origin of replication indicated by double arrow. Strain is EMB259. (n = 3 for all data points).



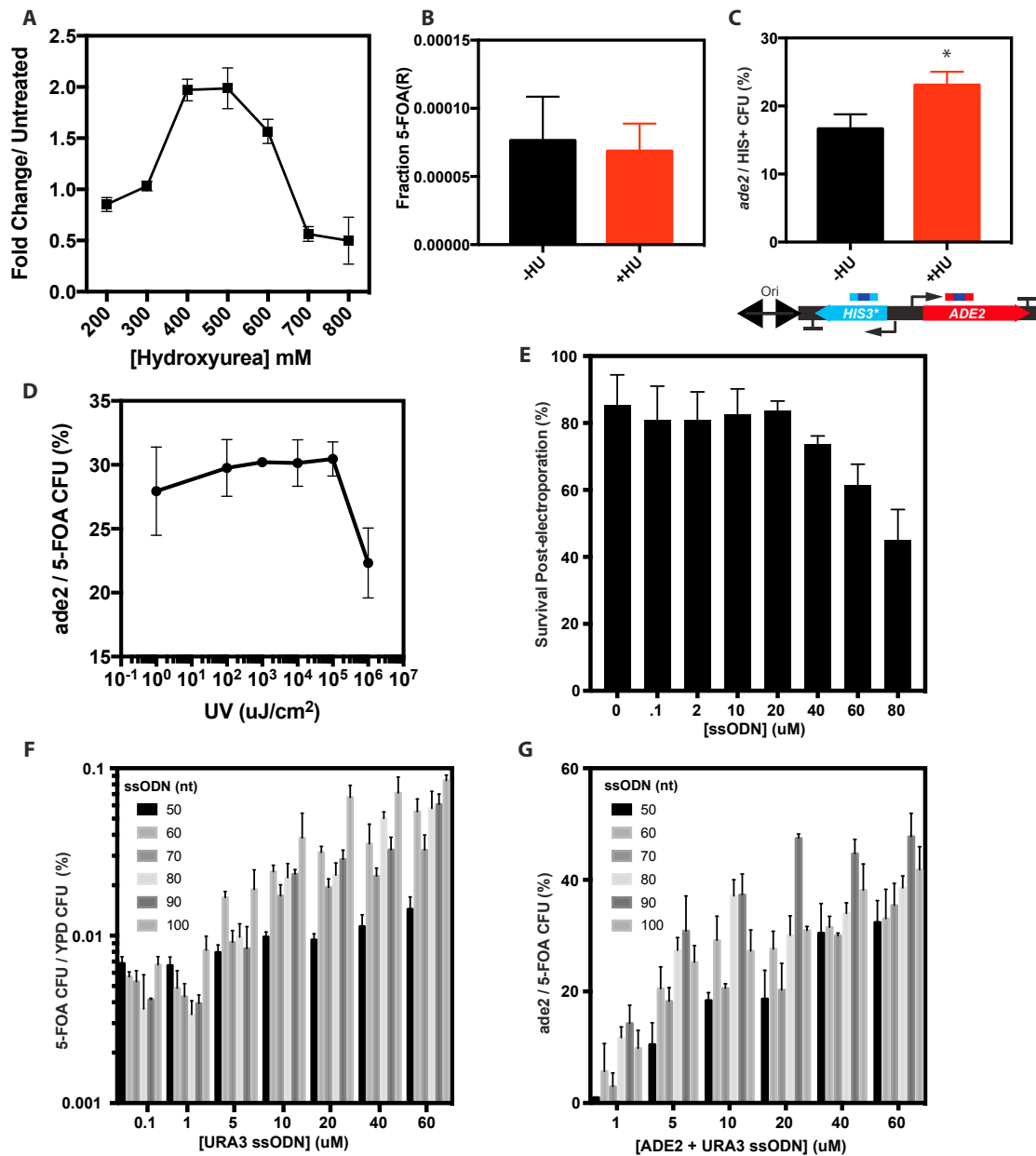


**Figure S2. Characterization of HU Treatment Conditions and ssODN Transformation Parameters in the *msh2Δ* Strain, Related to Figure 2**

(A) Concentration optimization for 30-minute HU treatment prior to electroporation with ssODNs targeting *URA3* and *ADE2*.

(B) Comparison of spontaneous 5-FOA resistant mutants  $\pm$  500mM HU treatment.

(C) The HU enhancement effect for recovering *ADE2* targeted mutants is observed when using a *HIS3* marker containing premature stop codon. Transformants are selected via the ssODN reversion of the *his3*<sup>+</sup> stop codon and subsequent selection on histidine auxotrophic media.

(D) Measurement of *ADE2* ARF after treatment with the indicated dose of UV irradiation.

(E) Characterization of cell survival post electroporation for a range of ssODN concentrations.

(F) The effect of ssODN size and concentration for single-plex targeting of the *URA3* marker. The number of 5-FOA resistant CFUs is normalized to CFUs on YPD (nonselective media). Cells are treated with 500mM HU.

(G) The effect of ssODN size and concentration for coupled targeting of *ADE2* and *URA3*. Shown is the number of *ade2* mutant (red) CFUs per 5-FOA resistant CFU. Cells are treated with 500mM HU. This is the same data that is represented in the heatmap showing the mean ARF in Figure 2C. N = 3 for all data.

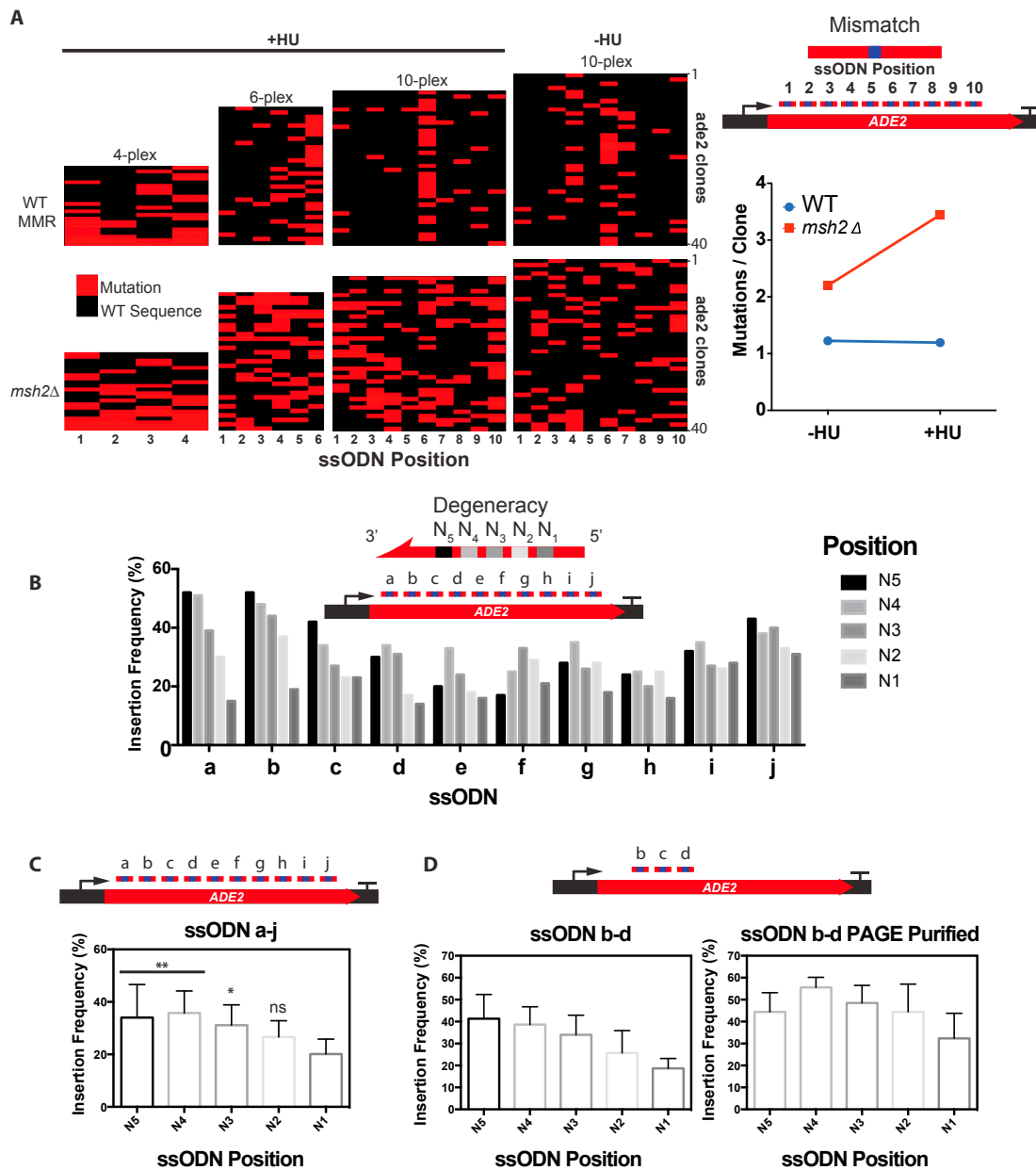


**Figure S3. Characterization of Multiplex Mutagenesis with ssODNs, Related to Figure 3**

(A) Color-maps indicating multiplex ssODN incorporation within the *ADE2* gene in WT and *msh2* strains. Data illustrates genotypes of *ade2* mutant clones resulting from multiplexed ssODN sets targeting 4, 6, or 10 target sites (4-plex, 6-plex, 10-plex) with HU treatment, and 10 ssODNs untreated (10-plex -HU). Clones are represented in rows, and the columns (indicated numerically) represent each ssODN target position across the *ADE2* gene. A red bar at a given position indicates incorporation of a targeted point mutation, and black indicates WT sequence at the locus. Notably, C-C mismatch mutations at position 6 were enriched by an average of 7.3-fold in WT cells, which is consistent with prior work showing that C-C mismatches evade MMR (Detloff et al., 1991). Number of clones sequenced (n), n = 22 (4 ssODNs), n = 32 (6 ssODNs), n = 36 (10 ssODNs), n = 40 (10 ssODNs -HU condition). 10-pex ± HU data is summarized on the adjacent plot as the average mutations per clone ± HU.

(B) Analysis of degenerate-insertion positional incorporation frequencies. Single cycle positional insertion frequencies for 10-plex ssODNs. The ssODNs are shown 3' to 5' to indicate directionality of incorporation at the lagging strand. Each ssODN is targeted to a distinct site within the *ADE2* gene indicated by a representative letter (a-j). Each insertion in the ssODN is indicated by "N" with subscript indicating the position of the insertion.

(C) Total insertion incorporation efficiency for all 10 ssODNs at each position within each ssODN from 100 clones sequenced after cycle 1. Statistical significance of 3' bias with ordinary one-way ANOVA comparison of individual positions N5-N2 with the 5' position being N1.

(D) The 3' bias trend was not statistically significant for ssODNs (b-d), however PAGE purification qualitatively reduced the 3' bias effect.

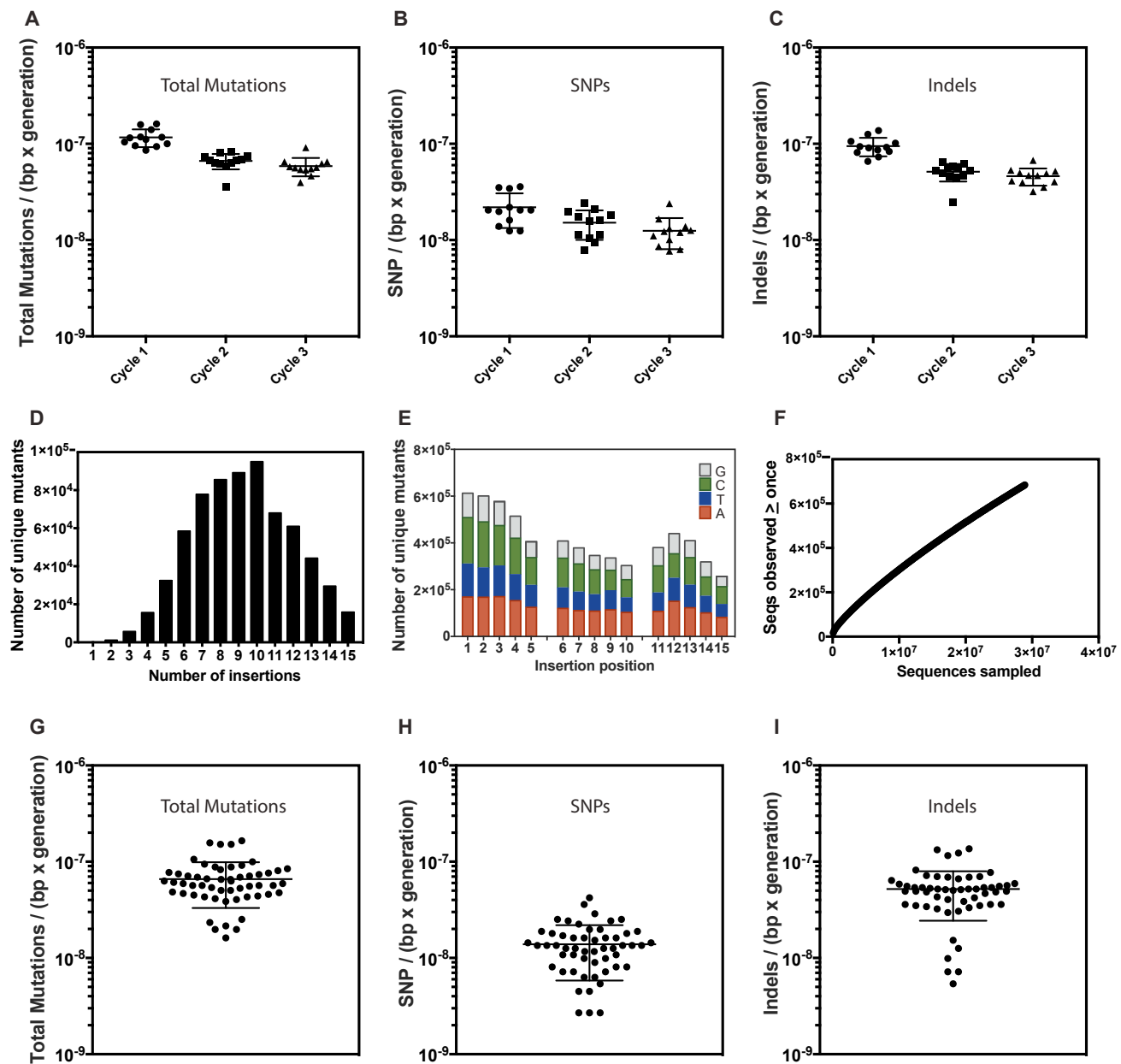


**Figure S4. WGS Analysis of Background Mutation Rates and HTS Analysis of Diversity Generated by eMAGE, Related to Figures 3–5**

- (A) Mutation rates for 12 *ade2* mutant clones per eMAGE cycle.  
 (B) SNP rates for 12 *ade2* mutant clones per eMAGE cycle.  
 (C) Indel rates for 12 *ade2* mutant clones per eMAGE cycle.  
 (D) Q20 distribution of insertion mutations observed.  
 (E) Q20 positional frequencies of insertion mutations within each ssODN.  
 (F) Rarefaction curve for Q20 quality score HTS reads.  
 (G) Mutation rates for 55 diversified  $\beta$ -carotene pathway clones.  
 (H) SNP rates for 55 diversified  $\beta$ -carotene pathway clones.  
 (I) Indel rates for 55 diversified  $\beta$ -carotene pathway clones.

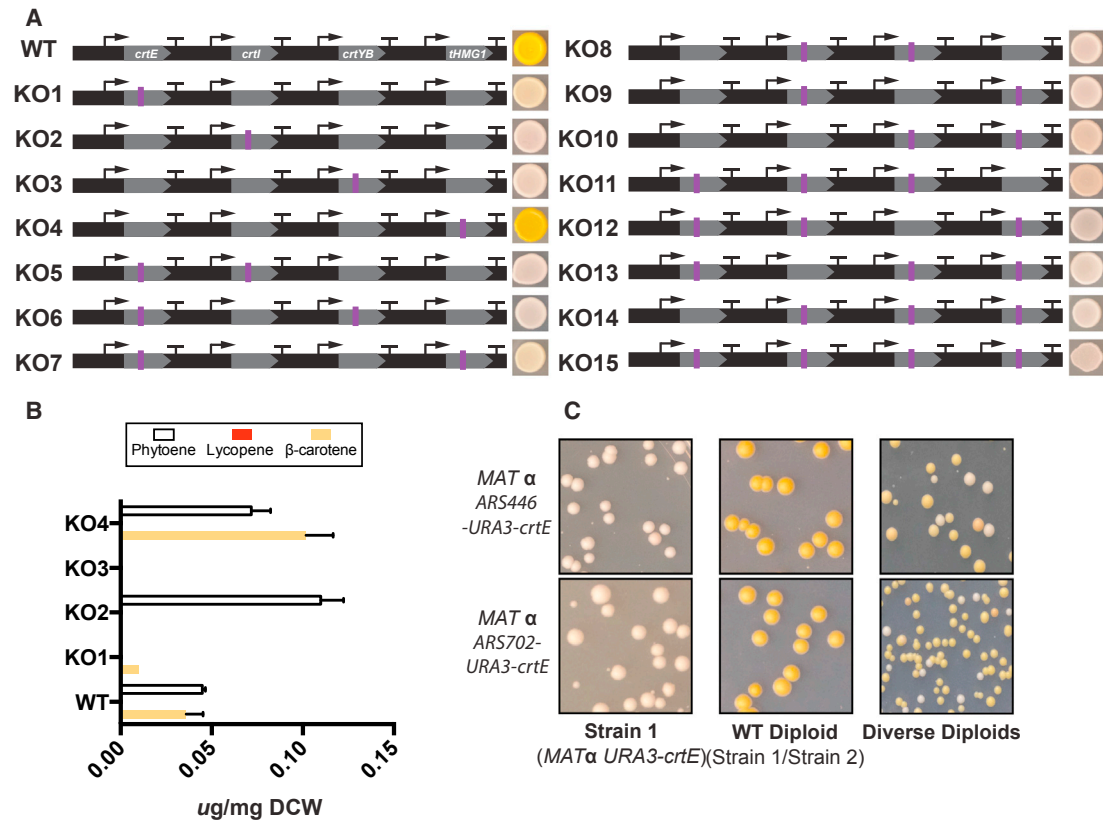


**Figure S5. Clonal Phenotypes for Combinatorial Gene Knockouts Set and Inter-chromosomal Targeting with Mating to Combine the Diversity between Haploid Strains, Related to Figures 5 and 6**

(A) Corresponding clone phenotype generated via a single ssODN transformation experiment.

(B) HPLC data for clonal production of  $\beta$ -carotene (orange) lycopene (red), and phytoene (white) ( $\mu\text{g}/\text{mg}$  dry cell weight). Values represent mean  $\pm$  SD for three replicates.

(C) Two *MAT $\alpha$*  haploids with *URA3-crtE* at *ARS446* on chromosome IV and *ARS702* on chromosome VII (Left most panel). Control cross with *MAT $\alpha$*  haploid containing the *crtI*, *crtYB*, and *tHMG1* at *ARS1516* (Middle panel). Cross of diversified *MAT $\alpha$*  and *MAT $\alpha$*  haploids (right most panel).

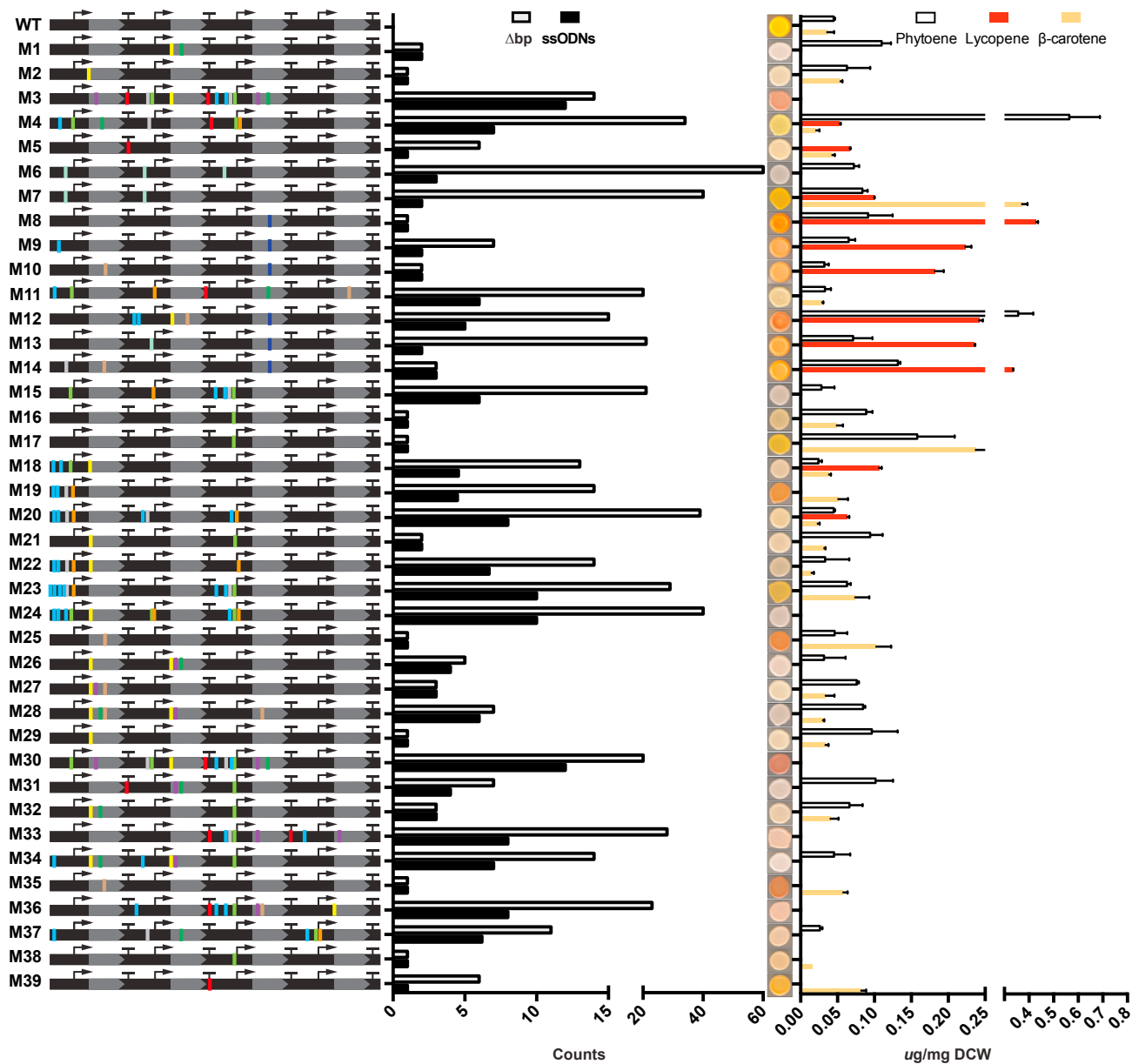


**Figure S6. Set of Clones Analyzed after Diversification, Related to Figure 5**

Genotypic and phenotypic analysis of variant clones after Sanger sequencing and HPLC analysis. Total number of ssODNs incorporated (black bar) and number of targeted base-pair changes (light-gray bar). HPLC data for clonal production of  $\beta$ -carotene (orange) lycopene (red), and phytoene (white) ( $\mu\text{g}/\text{mg}$  dry cell weight).



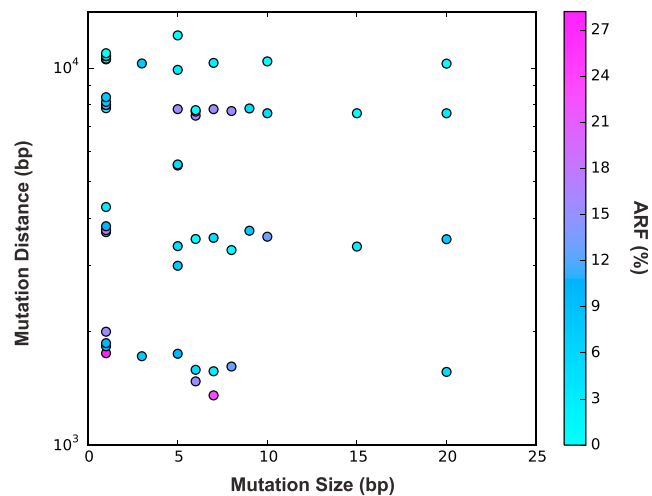


**Figure S7. Quantitative Data for ssODNs Used in Diversification, Related to Figure 5**

Quantitative data for ARFs associated with each ssODN. Heatmap represents the ARF determined by prevalence of ssODN-derived mutation at each target site for the clones analyzed.